European Journal of Mechanics / A Solids 113 (2025) 105678

Contents lists available at ScienceDirect

European Journal of Mechanics / A Solids

journal homepage: www.elsevier.com/locate/ejmsol

Full length article

A finite viscoelastic phase-field model for prediction of crack propagation speed in elastomers

Jacopo Ciambella [a], Giovanni Lancioni [b,*], Nico Stortini [b]

[a] Department of Structural and Geotechnical Engineering, Sapienza University of Rome, Rome, Italy
[b] Department of Civil and Building Engineering and Architecture, Polytechnic University of Marche, Ancona, Italy

ARTICLE INFO

Keywords:
Phase-field fracture
Finite viscoelasticity
Rubber fracture
Rate-dependent fracture toughness

ABSTRACT

Crack propagation in soft viscoelastic solids is crucial in many applications, yet accurate modeling of their fracture behavior, particularly the rate-dependent fracture toughness, remains a challenge. We address this by proposing a thermodynamically consistent phase-field fracture model for viscoelastic materials. The model incorporates both equilibrium and non-equilibrium elastic energies, along with distinct dissipation mechanisms for viscous losses and irreversible damage processes. Importantly, two characteristic time scales are introduced, reflecting the distinct nature of viscous relaxation and damage evolution, both of which significantly influence crack propagation dynamics. Numerical simulations are performed to investigate the impact of the different energy contributions on the fracture propagation in elastomeric membranes, accompanied by comparisons to experimental results.

1. Introduction

The fracture behavior of elastomers, as, in general, of viscoelastic materials, presents several complexities and theoretical challenges compared to their purely elastic counterparts (Knauss, 2015; Creton and Ciccotti, 2016). Unlike elastic solids, which preserve energy upon deformation, viscoelastic solids dissipate stored strain energy over time. This dissipation mechanism has been shown to significantly enhance the energy required per unit area of crack propagation (Schapery, 2022, 2023). Specifically, while elastic solids do not incur energy loss during energy transfer to the crack tip, elastomers and, in general, viscoelastic solids experience incomplete energy delivery, resulting in an apparent fracture toughness exceeding the intrinsic fracture toughness of the material. The disparity between these two values, termed viscoelastic dissipation, depends on crack propagation velocity due to the sensitivity of dissipative processes to stress and strain histories (Qi et al., 2024). Experimental investigations of fracture propagation in elastomeric samples have revealed distinct regimes of propagation, each characterized by specific crack propagation velocities (Chen et al., 2011; Mai et al., 2020; Morishita et al., 2016). These regimes are closely linked to microstructural effects occurring in the vicinity of the crack tip, and to rate-dependent strain processes in the bulk material, such as time-delayed crack lips opening. A detailed account of the experimental findings in this context is provided in Section 2.

Several theories have been proposed to describe fracture propagation in viscoelastic media, typically under the assumption of steady-state crack propagation and within the framework of linear viscoelasticity (Schapery, 2022; Persson and Brener, 2005). These theories commonly address the fracture process at the crack tip by either: prescribing an intrinsic fracture toughness, independent of the loading rate or deformation history, that is often used in models like the generalized Griffith criterion for viscoelastic solids (Schapery, 1975; Knauss, 1970); or by introducing a cohesive zone to model the fracture process zone as a finite region ahead of the crack tip where material separation occurs gradually. Cohesive zone models incorporate a traction-separation law to describe the forces resisting separation (Nguyen and Govindjee, 2006; Zreid et al., 2013; Cui et al., 2019).

Since the implementation of these theories is very intricate, their application usually restrict to the description of crack nucleating from a pre-existing crack, and propagating along a path a-priori known. An effective modeling approach that overcame these difficulties, is the phase-field fracture approach (Bourdin et al., 2000), originating from the variational formulation of brittle fracture (Francfort and Marigo, 1998). According to this approach, fracture is smeared over a region of finite width, and it is described by the phase-field variable, which is a smooth scalar field. This allows for a straightforward numerical implementation by using standard finite elements, eliminating the need for specialized enriched finite element methods. A further advantage

* Corresponding author.
E-mail address: g.lancioni@univpm.it (G. Lancioni).

https://doi.org/10.1016/j.euromechsol.2025.105678
Received 6 August 2024; Received in revised form 1 March 2025; Accepted 9 April 2025
Available online 24 April 2025

of the phase-field approach is that it can describe processes of crack nucleation and propagation without any knowledge of the crack path, by just solving a minimum problem.

The extension of the phase-field approach to finite elasticity was initially proposed in Del Piero et al. (2007), and several works followed later on. Among many, it is worth mentioning (Miehe and Schänzel, 2014; Talamini et al., 2018; Li and Bouklas, 2020) with fracture models based on the micro-mechanics of polymeric chains, Henao et al. (2016), Kumar et al. (2018) focused on the modeling of void coalescence and cavitation in elastomers, and Ciambella et al. (2022) for the modeling of pseudo-ductile fracture in double-layer elastomeric composites. Phase-field fracture was also extended to linear viscoelasticity (Dammaß et al., 2021), and finite viscoelasticity (Loew et al., 2019; da Costa-Haveroth et al., 2022; Dammaß et al., 2023; Yin and Kaliske, 2020) as well, to account of the rate-dependent nature of strains in elastomers. These studies showcase the adaptability of this approach in capturing various facets of fracture behavior. For instance, da Costa-Haveroth et al. (2022) utilizes fractional calculus to model intricate time-dependent behavior, while the authors of Dammaß et al. (2021, 2023) concentrate on unifying brittle and ductile fracture modes under finite deformation. Loew et al. (2019) emphasize experimental parameter identification for rubber, and Yin and Kaliske (2020) incorporate a history-dependent fracture toughness.

A recent series of papers by Shrimali and Lopez-Pamies (Shrimali and Lopez-Pamies, 2023b,a,c) revisited the notion of tearing energy, i.e., the energy supplied by the body to open a unit crack surface, in viscoelastic solids. In these works, the authors decompose elastic energy density into equilibrium and non-equilibrium components to model rate dependency and stress relaxation, and propose that, for pure shear specimens with pre-existing cracks, the critical energy release rate depends solely on the equilibrium, rate-independent part of the energy. This leads to a critical fracture stretch that is independent of the stretch rate in pure shear experiments on synthetic rubber. However, their model has sparked significant debate (Ciavarella, 2024; Persson et al., 2024), particularly regarding its broader applicability. Persson et al. Persson et al. (2024) point out that the experimental evidence supporting rate-independence is limited to conditions where the elastomer remains in its rubbery state. At significantly higher stretch rates, elastomers can enter their glassy regime, becoming more rigid and failing at lower critical stretches. More fundamentally, they argue there is no physical reason why the critical tearing energy should depend on strain rate and temperature in exactly the same way as the bulk viscoelastic modulus, since fracture involves distinct molecular processes like chain scission that are not involved in bulk viscoelasticity. Indeed, the broader experimental evidence shows that the effective rupture energy during steady-state crack propagation generally depends on crack velocity across a wide range of conditions (see Barthel (2024) for a recent review).

This paper contributes to this discussion by proposing a model that distinguishes between different dissipative mechanisms during crack propagation. Our variational formulation incorporates both stored strain energy and a dissipative potential that accounts for three distinct phenomena: crack opening, strain viscosity, and rate-dependent microprocesses associated with material failure. A key feature of our model is the introduction of two characteristic timescales: a damage timescale τ_{d} that governs processes near the crack tip (such as polymer chain rupture, void coalescence, and cavitation), and a bulk viscoelastic timescale τ_{v} that controls chain reconfiguration due to thermal fluctuations in the bulk material away from the crack. The governing equations are derived using an incremental variational principle, whereby the system evolves at each time step to minimize the total energy increment - defined as the difference between the incremental internal energy and the external work increment (Miehe and Schänzel, 2014).

The primary objective is to analyze how stored and dissipated energies affect fracture propagation. This analysis uses simplified forms for these energy contributions, minimizing the number of constitutive parameters to just three after normalization. While these simple constitutive assumptions limit the model's predictive capabilities, they enable clear understanding of how different energy contributions influence fracture propagation rates. The study includes comprehensive parametric analysis to validate against experimental data from both cutting tests on pre-stretched membranes (Mai et al., 2020; Morishita et al., 2016; Corre et al., 2020) as well as on rupture of pre-notched samples (Cristiano et al., 2011; Pharr et al., 2012; Wang et al., 2017).

The paper is structured as follows. Section 2 outlines the main features observed in the response during crack deformation experiments, with the aim of incorporating these effects into a continuum model. The model derivation is carried out in Section 3, while its specific features are explored in Section 4 with reference to the 1D problem of a viscoelastic bar. Section 5 is dedicated to applying the model to capture the fracture behavior of viscoelastic membranes observed in the experiments.

2. Phenomenology of crack propagation

The propagation of cracks in elastomers involves a complex interplay of factors, including material properties, strain rates, and energy dissipation mechanisms. To investigate continuous crack growth in elastomers, two experimental approaches are usually employed: (i) *relaxed sample cutting*, and (ii) *pre-cracked sample deformation*.

The former setup is sketched in Fig. 1(a)–(c) for a membrane, whose aspect ratio ($\ell \gg b$) is chosen to guarantee the specimen to be under a state of pure shear. Initially, the elastomer sample is pre-stretched to a desired strain level λ_{pre} and allowing it to relax until it reaches a quasi-equilibrium state. Once relaxed, a sharp cut is introduced into the sample to initiate a crack. Subsequent crack growth is then monitored while keeping the overall strain constant. The initial relaxation step minimizes the effects of residual stresses and provides a better understanding of the role of viscoelasticity in crack propagation. Additionally, this approach enables the investigation of crack growth behavior at different levels of pre-stretch, offering insights into the effects of stored energy in the sample on crack propagation speed.

The results of the *relaxed sample cutting test*, illustrated in Fig. 2 using data from Mai et al. (2021), show the steady-state crack propagation speed in terms of prestretch level λ_{pre} and tearing energy Γ, i.e., the energy per unit of fractured area expended in the tearing process, calculated from the experimental stress–strain curve. The material used in these experiments is carbon black filled styrene-butadiene rubber, but similar qualitative behavior has been consistently observed across different elastomers, both synthetic (Morishita et al., 2016; Corre et al., 2020; Kubo et al., 2021) and natural rubber (Chen et al., 2011; Kubo et al., 2021). The data reveals an abrupt transition in crack growth rate within a narrow range of tearing energy or prestretch, distinguishing two regimes of crack propagation: a "slow mode" with very slow crack speeds (10^{-5}–10^{-3} m/s) and a "fast mode" with significantly higher speeds (10^{-1}–10^{2} m/s).

In the slow mode, the crack speed exhibits no clear dependence on the tearing energy. In contrast, in the fast mode, a power-law relationship emerges, with the crack speed scaling with either the tearing energy or the pre-stretch. The transition threshold from slow to fast mode is influenced by several factors, including the type of elastomer, filler content, cross-link density, and temperature. At very high energy levels, the crack speed can even exceed the shear wave speed of the material, leading to a regime often referred to as supershear or intersonic crack propagation (Corre et al., 2020; Kamasamudram et al., 2021). This regime is essentially determined by the strain hardening properties of elastomers, which exhibit a significant increase in the equivalent shear modulus at large strains and high deformation rates. In addition, inertial effects become significant, as the rubber networks lack sufficient time to efficiently transfer energy to the area surrounding the crack tip. As a result, the rubber networks within the

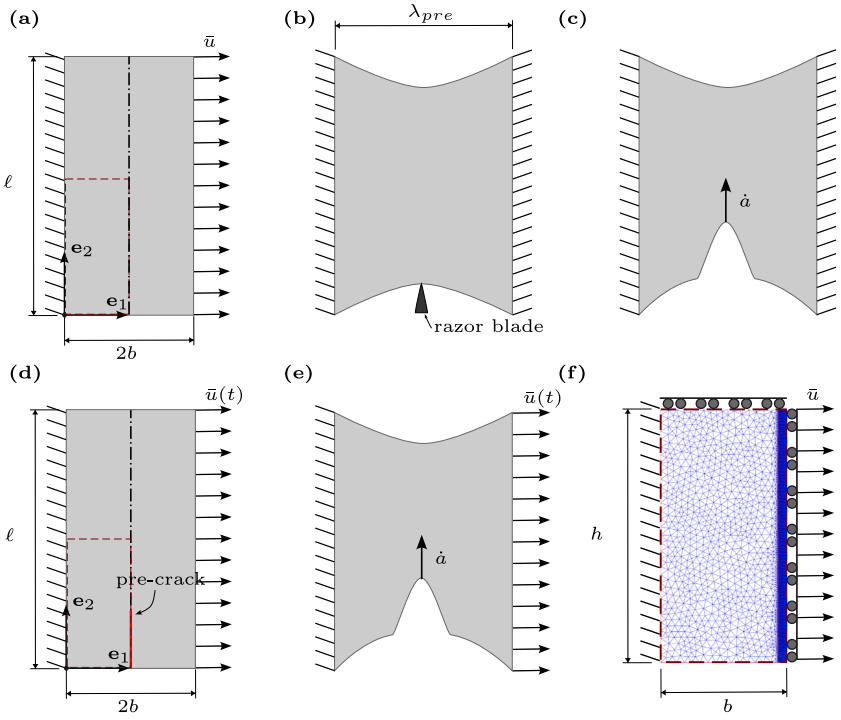

Fig. 1. Experimental setups for relaxed sample cutting (a)–(c) and pre-notched specimen rupture (d)–(e); computational domain (f) exploiting the symmetry of the specimen, together with details of the mesh refinement in the crack region ($\ell > h \gg b$).

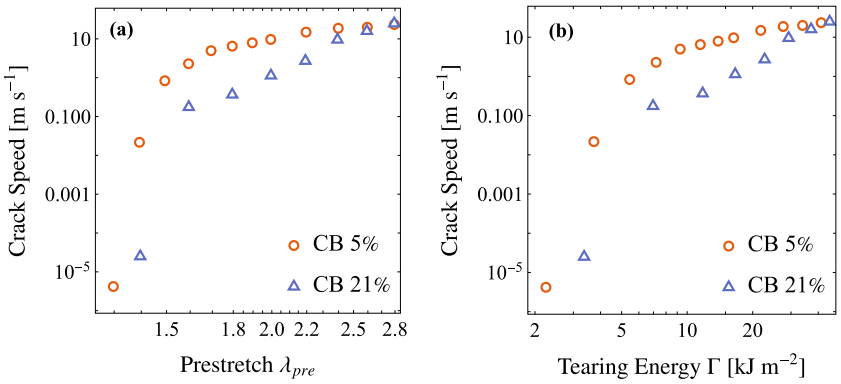

Fig. 2. Steady-state crack growth velocity as a function of pre-stretch λ_{pre} (a) and tearing energy Γ (b) for SBR rubber with different carbon black content. *Source:* Data from Mai et al. (2021).

damage zone experience rapid rupture, akin to a shock-like fracture, with minimal viscoelastic dissipation.

Another interesting feature highlighted in several studies is the relationship between crack profiles and crack speed. In the slow mode, crack tip profiles are generally observed to be blunt and close to parabolic, as predicted by linear elastic fracture mechanics. However, as the crack speed increases, especially in the fast mode, the crack tip becomes progressively sharper, deviating significantly from the parabolic prediction (Morishita et al., 2016; Mai et al., 2020; Corre et al., 2020). This deviation has been attributed to several factors, including the nonlinear elastic response of the elastomer, which stiffens at high strains, and the distinct characteristics of the viscoelastic response. However, a definitive explanation remains elusive.

In addition to the experimental setup described previously, another approach (ii) involves introducing a pre-existing crack or notch into the elastomer sample before applying any load (Fig. 1(d)–(e)). The specimen is then subjected to controlled deformation, such as uniaxial tension or pure shear, until complete rupture occurs. This method enables the direct observation of the deformation at which crack starts propagating in terms of different loading conditions, in particular loading rate. Indeed, this loading rate introduces an additional time scale that affects the elastomer's viscoelastic response, potentially leading to distinct characteristics in the crack propagation behavior (Wang et al., 2023).

The primary focus of this paper is to develop a modeling approach capable of accurately predicting crack propagation speeds in the fast mode regime, specifically well below the Rayleigh wave speed so that inertial effects can be neglected. In this regime, the interplay between viscoelasticity and crack propagation, which is the main subject of this study, plays the most significant role. Both the experimental setups will be simulated in Section 5.

3. Model formulation

In this section, we introduce the primary equations governing the model.

We employ small bold letters (**a**, **b**) to denote vectors, while capital bold letters (**A**, **B**) tensors. The cartesian orthonormal base $\mathbf{e}_1$, $\mathbf{e}_2$, and

$\mathbf{e}_3$ is utilized, with the components of vector $\mathbf{a}$ denoted as $a_i = \mathbf{a} \cdot \mathbf{e}_i$, where $\cdot$ denotes the inner product between vectors. For tensors, the components are expressed as $\mathbf{A} \cdot \mathbf{e}_i \otimes \mathbf{e}_j = A_{ij}$, with $\cdot$ representing the inner product between tensors, defined by $\mathbf{A} \cdot \mathbf{B} = \mathrm{tr}(\mathbf{A}\mathbf{B}^T)$. An overdot indicates the material time derivative, while a prime denotes the derivative with respect to the independent variable (e.g., position x or variable d). The symbol $\otimes$ denotes the dyadic product between vectors, defined as $(\mathbf{a} \otimes \mathbf{b})_{ij} = a_i b_j$.

For conciseness, explicit time dependence is omitted from all fields unless required for clarity. In such cases, a subscript t, as in $(\cdot)_t$, denotes the variable's dependence on time.

3.1. State variables, energy and dissipation

Let Ω_0 denote the reference configuration at the initial instant $t = 0$, and let $X \in \Omega_0$ represent a material point. The current configuration at time t is given by $\Omega = \chi(\Omega_0)$ and $x = \chi(X) \in \Omega$. Adopting a Lagrangean approach to the equilibrium problem, we define a thermodynamic process by the state variables at any material point X and time t, given by

$$\{\mathbf{u}(X), d(X), \mathbf{C}_{\mathrm{v}}(X)\}.$$

Here, $\mathbf{u}(X) = \chi(X) - X$ represents the displacement vector field of point X; $d(X)$ is a scalar phase-field variable, $0 \le d \le 1$, that is 0 for the neat material and 1 when fully damaged; $\mathbf{C}_{\mathrm{v}}(X)$ is a symmetric second-order positive definite unimodular tensor ($\det \mathbf{C}_{\mathrm{v}} = 1$) that quantifies the viscous deformation at a point X. It captures the discrepancy between the macroscopic deformation of the polymer network and its relaxed configuration. The unimodularity constraint on $\mathbf{C}_{\mathrm{v}}$ implies that viscoelastic effects related to volume changes (bulk modulus) are neglected in this theory, a common and experimentally validated assumption in rubber viscoelasticity.

The displacement field $\mathbf{u}(X) = \mathbf{u}^*$ is assigned on the portion of the boundary $\partial\Omega_0^u$, complementary to $\partial\Omega_0^t$ where surface loads are applied ($\partial\Omega_0^u \cup \partial\Omega_0^t = \partial\Omega_0$, $\partial\Omega_0^u \cap \partial\Omega_0^t = \emptyset$).

Since the governing equations of the problem will be derived through an incremental variational approach on the state variable rates $\{\dot{\mathbf{u}}, \dot{d}, \dot{\mathbf{C}}_{\mathrm{v}}\}$, it is beneficial to introduce the space of admissible variations $\{\delta\dot{\mathbf{u}}, \delta\dot{d}, \delta\dot{\mathbf{C}}_{\mathrm{v}}\}$ in

$$\begin{aligned}
\delta\dot{\mathcal{U}} &= \{\delta\dot{\mathbf{u}} \ : \ \delta\dot{\mathbf{u}}(X) = 0, \forall\, X \in \partial\Omega_0^u\}\,,\\
\delta\dot{\mathcal{D}} &= \{\delta\dot{d} \ : \ \dot{d}(X) + \delta\dot{d}(X) \ge 0 \text{ a.e. in } \Omega_0,\ \forall\, \dot{d}\}\,,\\
\delta\dot{\mathcal{V}} &= \{\delta\dot{\mathbf{C}}_{\mathrm{v}} \ : \ \delta\dot{\mathbf{C}}_{\mathrm{v}} \cdot \mathbf{C}_{\mathrm{v}}^{-1} = 0, \forall X \in \Omega_0,\ \forall\, \mathbf{C}_{\mathrm{v}}\}\,,
\end{aligned}$$

with latter condition stems from the fact that the unimodularity of $\mathbf{C}_{\mathrm{v}}$ implies $\dot{\mathbf{C}}_{\mathrm{v}} \cdot \mathbf{C}_{\mathrm{v}}^{-1} = 0$, such that

$$(\dot{\mathbf{C}}_{\mathrm{v}} + \delta\dot{\mathbf{C}}_{\mathrm{v}}) \cdot \mathbf{C}_{\mathrm{v}}^{-1} = 0\,.$$

On the other hand, the condition on the damage irreversibility $\dot{d} \ge 0$, that prevent damage healing, gives

$$\dot{d} + \delta\dot{d} \ge 0$$

and in particular

$$\begin{aligned}
&\dot{d} = 0 \quad \Rightarrow \quad \delta\dot{d} \ge 0\\
&\dot{d} > 0 \quad \Rightarrow \quad \delta\dot{d} \gtrless 0\,.
\end{aligned} \tag{1}$$

In order to derive the governing equation of the problem we follows the generalized standard materials approaches developed in Halphen et al. (1975). To this end, we introduce two functionals related to energy storage and dissipative mechanisms, respectively. The functional

$$\mathcal{F} = \int_{\Omega_0} \Psi\,, \quad \text{with} \quad \Psi = \Psi(\nabla\mathbf{u}, d, \mathbf{C}_{\mathrm{v}})\,, \tag{2}$$

represents the energy stored during a thermodynamic process, with Ψ the elastic strain energy density that depends on the deformation $\mathbf{F} = \nabla\mathbf{u}$, the phase field variable d and the viscous strain $\mathbf{C}_{\mathrm{v}}$. Furhtermore, the functional

$$\mathcal{D} = \int_{\Omega_0} \phi\,, \quad \text{with} \quad \phi = \phi(d, \dot{d}, \nabla d, \nabla\dot{d}, \dot{\mathbf{C}}_{\mathrm{v}})\,,$$

represents the power associated to internal dissipation mechanisms. In particular, the dissipation potential ϕ depends on d, its gradient ∇d, and their respective rates, $\dot{d}$ and $\nabla\dot{d}$, as well as on $\dot{\mathbf{C}}_{\mathrm{v}}$, which is associated with bulk dissipation in the undamaged material. The inclusion of d, $\dot{d}$, ∇d, and $\nabla\dot{d}$ in the dissipation potential accounts for the energy dissipation due to the formation and growth of cracks within the material (Miehe et al., 2010). In rate-independent systems, $\mathcal{D}$ directly corresponds to the dissipation rate. However, for rate-dependent systems, the relationship between $\mathcal{D}$ and the actual physical dissipation can be more intricate (Miehe, 2011).

To ensure thermodynamic consistency and material stability, we posit that both Ψ and ϕ are convex functions of the appropriate strain measures and internal variables.

3.2. Incremental variational principle

In this section, the governing equations of the evolution problem are established in an incremental setting by enforcing the non-negativeness of the first variation of the total energy increment. This incremental approach aligns with the methodology employed in previous studies on elasto-plastic materials (Miehe, 2011; Del Piero et al., 2013, 2023).

For notation convenience, we will consider all variables without a subscript to be evaluated at time $t + \tau$, where τ is the time increment. We define

$$\mathbf{u} = \mathbf{u}_t + \tau\,\dot{\mathbf{u}}, \qquad d = d_t + \tau\,\dot{d}, \qquad \mathbf{C}_{\mathrm{v}} = \mathbf{C}_{\mathrm{v}_t} + \tau\,\dot{\mathbf{C}}_{\mathrm{v}},$$

thus, $\mathbf{u}$, d and $\mathbf{C}_{\mathrm{v}}$ represent the displacement field, the damage field and viscous deformation tensor at time $t + \tau$, respectively. Given the configuration $\{\mathbf{u}_t, d_t, \mathbf{C}_{\mathrm{v}_t}\}$ of the system at time t, the configuration at time $t + \tau$ is obtained from the above expressions by determining the rates $\{\dot{\mathbf{u}}, \dot{d}, \dot{\mathbf{C}}_{\mathrm{v}}\}$. The governing equations for these rates are variationally deduced by using a minimum principle that operates on the total energy increment in the interval $(t, t + \tau)$ (Ichiyanagi, 1994). We define the total energy increment

$$\Pi(\dot{\mathbf{u}}, \dot{d}, \dot{\mathbf{C}}_{\mathrm{v}}) = \Delta\mathcal{E}_{int}(\dot{\mathbf{u}}, \dot{d}, \dot{\mathbf{C}}_{\mathrm{v}}) - \Delta\mathcal{E}_{ext}(\dot{\mathbf{u}})\,,$$

in terms of the incremental internal energy (stored and dissipated)

$$\Delta\mathcal{E}_{int} = \int_{\Omega_0} (\Psi - \Psi_t) + \tau \int_{\Omega_0} \phi\,, \tag{3}$$

and the incremental external energy

$$\Delta\mathcal{E}_{ext} = \int_{\Omega_0} \mathbf{b} \cdot (\mathbf{u}_t + \tau\dot{\mathbf{u}}) - \mathbf{b}_t \cdot \mathbf{u}_t + \int_{\partial\Omega_0^t} \mathbf{t} \cdot (\mathbf{u}_t + \tau\dot{\mathbf{u}}) - \mathbf{t}_t \cdot \mathbf{u}_t\,,$$

where $\mathbf{b}$ and $\mathbf{t}$ represent the body forces and surface tractions per unit reference volume and area, respectively, that are assumed to be independent on the state variables (dead loads).

The minimum principle to be satisfied states that the net energy expenditure Π within the interval $(t, t + \tau)$ attains a minimum in an evolution process (Miehe, 2011; Ichiyanagi, 1994). Necessary condition for a minimum of Π is that the first variation be non-negative for any admissible perturbation of the state variables

$$\delta\Pi(\dot{\mathbf{u}}, \dot{d}, \dot{\mathbf{C}}_{\mathrm{v}})[\delta\dot{\mathbf{u}}, \delta\dot{d}, \delta\dot{\mathbf{C}}_{\mathrm{v}}] \ge 0\,, \qquad \forall\ \delta\dot{\mathbf{u}} \in \delta\dot{\mathcal{U}},\ \delta\dot{d} \in \delta\dot{\mathcal{D}},\ \delta\dot{\mathbf{C}}_{\mathrm{v}} \in \delta\dot{\mathcal{V}},$$

that yields

$$\begin{aligned}
\frac{1}{\tau}\delta\Pi(\dot{\mathbf{u}}, \dot{d}, \dot{\mathbf{C}}_{\mathrm{v}}; \delta\dot{\mathbf{u}}, \delta\dot{d}, \delta\dot{\mathbf{C}}_{\mathrm{v}}) = \int_{\Omega_0} \Big(\frac{\partial\Psi}{\partial\nabla\mathbf{u}} \cdot \nabla\delta\dot{\mathbf{u}} + \frac{\partial\Psi}{\partial d}\,\delta\dot{d} + \frac{\partial\Psi}{\partial\mathbf{C}_{\mathrm{v}}} \cdot \delta\dot{\mathbf{C}}_{\mathrm{v}} \Big) +\\
+ \int_{\Omega_0} \Big(\frac{\partial\phi}{\partial\dot{d}}\,\delta\dot{d} + \frac{\partial\phi}{\partial\nabla\dot{d}} \cdot \nabla\delta\dot{d} + \frac{\partial\phi}{\partial\dot{\mathbf{C}}_{\mathrm{v}}} \cdot \delta\dot{\mathbf{C}}_{\mathrm{v}} \Big) - \int_{\Omega_0} \mathbf{b} \cdot \delta\dot{\mathbf{u}} - \int_{\Omega_0} \mathbf{t} \cdot \delta\dot{\mathbf{u}} \ge 0\,.
\end{aligned}$$

Applying Gauss' theorem to the gradient terms in the first two integrals yields

$$\int_{\Omega_0} \left(-\mathrm{Div}\,\frac{\partial \Psi}{\partial \nabla \mathbf{u}} - \mathbf{b}\right)\cdot \delta\dot{\mathbf{u}} + \int_{\partial\Omega_0} \left(\frac{\partial \Psi}{\partial \nabla \mathbf{u}}\mathbf{n} - \mathbf{t}\right)\cdot \delta\dot{\mathbf{u}} + \int_{\Omega_0} \left(\frac{\partial \Psi}{\partial \mathbf{C}_\mathrm{v}} + \frac{\partial \phi}{\partial \dot{\mathbf{C}}_\mathrm{v}}\right)\cdot \delta\dot{\mathbf{C}}_\mathrm{v} - \int_{\Omega_0} Y\,\delta\dot{d} + \int_{\partial\Omega_0} \frac{\partial \phi}{\partial \nabla \dot{d}}\cdot \mathbf{n}\delta\dot{d} \geq 0, \tag{4}$$

where $\mathbf{n}$ is the outward unit normal to $\partial\Omega_0$, and

$$Y = \mathrm{Div}\,\frac{\partial \phi}{\partial \nabla \dot{d}} - \frac{\partial \Psi}{\partial d} - \frac{\partial \phi}{\partial \dot{d}} \tag{5}$$

is the thermodynamic force conjugate to $\dot{d}$, also called *damage yielding function*.

Given the arbitrariness of $\delta\dot{\mathbf{u}}$, we obtain the following macroscopic balance equation:

$$\mathrm{Div}\,\mathbf{P} + \mathbf{b} = \mathbf{0}, \quad \text{in} \quad \Omega_0 \qquad \text{and} \qquad \mathbf{P}\mathbf{n} = \mathbf{t}, \quad \text{on} \quad \partial\Omega_0^t\,. \tag{6}$$

in which the stress tensor $\mathbf{P} = \partial\Psi/\partial\nabla\mathbf{u}$ is usually referred to as first-Piola Kirchhoff stress. Concerning the third integral in (4), we can relax the requirement $\delta\dot{\mathbf{C}}_\mathrm{v}\cdot\mathbf{C}_\mathrm{v}^{-1} = 0$ by introducing a Lagrange multiplier $q\,\mathbf{C}_\mathrm{v}^{-1}$ in the integrand, allowing $\delta\dot{\mathbf{C}}_\mathrm{v}$ to be arbitrary. Consequently, the integral can be localized as follows:

$$\frac{\partial \phi}{\partial \dot{\mathbf{C}}_\mathrm{v}} + \frac{\partial \Psi}{\partial \mathbf{C}_\mathrm{v}} - q\,\mathbf{C}_\mathrm{v}^{-1} = 0, \quad \text{in} \quad \Omega_0. \tag{7}$$

This equation represents Biot's equation for the evolution of the internal-like variable $\mathbf{C}_\mathrm{v}$, where q serves as a reactive stress-like variable required to maintain the unimodularity of $\mathbf{C}_\mathrm{v}$.

Finally, on assuming that the derivative $\partial\phi/\partial\nabla\dot{d}$ vanishes on the boundary, the remaining integrals in (4) together with the conditions (1) on the damage variations, gives the KKT conditions for the damage evolution problem, i.e.

$$\dot{d} \geq 0, \qquad Y \leq 0, \qquad Y\,\dot{d} = 0\,. \tag{8}$$

3.3. Constitutive assumptions

In this section, specific forms are assigned to the densities Ψ and ϕ that govern the constitutive response of the continuum. To ensure objectivity, these functions must remain invariant under superimposed rigid body motions.

Elastic energy density. Within the classical phase field framework, the elastic energy is decremented by damage through a degradation function g_ψ:

$$\Psi(\nabla\mathbf{u}, d, \nabla d, \mathbf{C}_\mathrm{v}) = g_\psi(d)\,\psi(\mathbf{C}, \mathbf{C}_\mathrm{v})\,, \tag{9}$$

where ψ is the elastic energy of the neat material. The degradation function must satisfy the condition $g_\psi'(d) < 0$, $g_\psi(0) = 1$, $g_\psi(1) = 0$. and $g_\psi'(0) = 0$. We make the common choice

$$g_\psi(d) = (1-d)^2\,. \tag{10}$$

For what concerns the elastic energy density of the neat material, frame invariance leads on writing ψ as a function of the right Cauchy–Green strain tensor $\mathbf{C} = \mathbf{F}^T\mathbf{F}$ rather than the deformation $\mathbf{F} = \nabla\mathbf{u}$ as introduced in (9).

To capture viscoelastic effects, we decompose ψ (energy density per unit of reference volume) as the sum of two components: the *equilibrium* component ψ_eq, which is assumed to depend on the macroscopic deformation, i.e., $\psi_\mathrm{eq}(\mathbf{C})$, and the *non-equilibrium* component, which depends both on the macroscopic $\mathbf{C}$ and on the viscous deformation, i.e., $\psi_\mathrm{neq}(\mathbf{C}, \mathbf{C}_\mathrm{v})$. Formally, one has

$$\psi(\mathbf{C}, \mathbf{C}_\mathrm{v}) = \psi_\mathrm{eq}(\mathbf{C}) + \psi_\mathrm{neq}(\mathbf{C}, \mathbf{C}_\mathrm{v})\,. \tag{11}$$

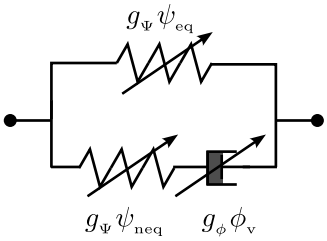

Fig. 3. Rheological elements underpinning the constitutive assumptions employed in the model. Both the equilibrium and non-equilibrium energy densities, as well as the dissipation density, are attenuated by damage d through distinct degradation functions g_ψ and g_ϕ.

The equilibrium component ψ_eq represents the energy stored in the material's relaxed state under a given deformation, governing long-term, reversible elastic behavior. The non-equilibrium component ψ_neq captures energy associated with ongoing internal reconfigurations (chain disentanglement, inter-chain friction, and transient bond dynamics) that have yet to reach equilibrium. This component dictates time-dependent viscoelastic responses like stress relaxation and energy dissipation (hysteresis). With definitions (9) and (11) on hand, the first-Piola Kirchhoff stress tensor $\mathbf{P}$ that appears in the balance Eq. (6) is constitutively rewritten as

$$\mathbf{P} = \mathbf{P}_\mathrm{eq} + \mathbf{P}_\mathrm{neq}\,,$$

with

$$\mathbf{P}_\mathrm{eq} = 2\,g_\psi(d)\,\mathbf{F}\frac{\partial \psi_\mathrm{eq}}{\partial \mathbf{C}}(\mathbf{C}), \qquad \mathbf{P}_\mathrm{neq} = 2\,g_\psi(d)\,\mathbf{F}\frac{\partial \psi_\mathrm{neq}}{\partial \mathbf{C}}(\mathbf{C}, \mathbf{C}_\mathrm{v}). \tag{12}$$

Remark. This approach, shared by various finite viscoelasticity theories (Califano and Ciambella, 2023; Ciambella et al., 2024; Reese and Govindjee, 1998; Sadik and Yavari, 2023) is indeed closely related to the rheological-like element in Fig. 3. At small deformations, the equilibrium and non-equilibrium energies correspond to the energy stored in the two springs during deformation. These energy components, ψ_eq and ψ_neq have distinct natural states: when $\mathbf{C} = \mathbf{I}$, then $\psi_\mathrm{eq}(\mathbf{I}) = 0$, indicating that the reference configuration must be a natural state for ψ_eq. Conversely, when $\mathbf{C}_\mathrm{v} = \mathbf{C} \neq \mathbf{I}$, $\psi_\mathrm{neq}(\mathbf{C}, \mathbf{C}^{-1}) = 0$, the non-equilibrium energy vanishes, meaning that the natural state for the non-equilibrium energy is when the viscous deformation matches the total deformation, even if the material is deformed.

Dissipation density. Energy dissipation plays a pivotal role in enhancing fracture toughness in viscoelastic solids, particularly around propagating cracks.

To capture this effect, we model the dissipation density ϕ as the sum of three components:

$$\phi(d, \dot{d}, \dot{\mathbf{C}}_\mathrm{v}) = G_c\,\left(\frac{3}{2\ell_f}\dot{d} + \frac{3\ell_f}{16}\nabla d\cdot\nabla\dot{d}\right) + \tau_\mathrm{d}\frac{3G_c}{4\ell_f}\,\dot{d}^2 + g_\phi(d)\,\phi_\mathrm{v}(\dot{\mathbf{C}}_\mathrm{v})\,, \tag{13}$$

where G_c is the rate-independent fracture toughness and ℓ_f is the width of the damaged region measured in a simple tensions experiment (Ciambella et al., 2022). Here, the first term takes into account dissipation related to bond scission. It is sum of a linear term proportional to $\dot{d}$ and a non-local contribution smearing damage over a region of amplitude ℓ_f. The second term, quadratic with respect to $\dot{d}$, describes time-dependent processes, governed by the characteristic time τ_d occurring in the damaging zone (the so-called *process zone*), such as cavity formation, stringing, chain pull-out (Persson et al., 2005; Wang et al., 2023; Barthel, 2024). The third and last term represents the viscous dissipation in the bulk material arising from the inherent

dynamics of the polymer chains.[1] The function $\phi_{\rm v}$ is modulated with a degradation function $g_\phi(d)$, that, consistently with the degradation function g_ψ employed for the elastic energy, is assumed to satisfy the conditions: $g_\phi'(d) < 0$, $g_\phi(0) = 1$, $g_\phi(1) = 0$, and $g_\phi'(0) = 0$. Indeed, the latter term in (13), describes viscous dissipation only in the bulk material, and not in the fracture process zone, where polymer chains are fully extended and unable to slide, thereby impeding viscous losses. Time-delay phenomena, which are different in nature from those producing viscous strain, are modeled by the quadratic term in $\dot d$.

With definitions (9) and (13), the damage yielding function (5) becomes

$$Y = \frac{3}{16}\, G_c\, \ell_f\, \Delta d - g_\psi'(d)(\psi_{\rm eq} + \psi_{\rm neq}) - \frac{3\, G_c}{2\, \ell_f}(\tau_{\rm d}\, \dot d + 1),$$

and, on accounting for the definition of the degradation function (10), we rewrite the KKT conditions (8) as

$$\dot d = \frac{1}{\tau_{\rm d}} \Big\langle \frac{1}{8}\, \ell_f^2\, \Delta d + \frac{4\, \ell_f}{3\, G_c}\, (1-d)\, (\psi_{\rm eq} + \psi_{\rm neq}) - 1 \Big\rangle, \tag{14}$$

where the Macaulay brackets are used ($\langle x\rangle = 0$ if $x < 0$, $\langle x\rangle = x$ if $x \geq 0$). Eq. (14) represents the evolution equation of the damage variable. On the other hand, the evolution of the inelastic variable is obtained from (7) as

$$g_\phi(d)\, \frac{\partial \phi_{\rm v}}{\partial \dot{\mathbf{C}}_{\rm v}} + g_\psi(d)\, \frac{\partial \psi_{\rm neq}}{\partial \mathbf{C}_{\rm v}} - q\, \mathbf{C}_{\rm v}^{-1} = \mathbf{0} \tag{15}$$

that requires the specification of the elastic energy density and the dissipation density.

In the context of elastomeric materials, we can exploit their inherent incompressibility. This constraint is incorporated into our model by introducing a Lagrange multiplier p into the elastic energy Ψ in (9)

$$\Psi = g_\psi(d)(\psi_{\rm eq} + \psi_{\rm neq}) - p\,(I_3^{1/2} - 1)$$

with $I_3 = \det \mathbf{C}$. In this approach the pressure term is independent on damage meaning that the bulk modulus remains sufficiently large in the damage state compared to the apparent shear modulus that is indeed reduced upon occurrence of damage. The equilibrium and non-equilibrium energy densities are assumed in the following neo-Hookean-like forms

$$\begin{aligned} \psi_{\rm eq}(\mathbf{C}) &= \frac{\mu_{\rm eq}}{2}\big(I_3^{-1/3}\mathbf{C}\cdot\mathbf{I} - 3\big) \\ \psi_{\rm neq}(\mathbf{C}, \mathbf{C}_{\rm v}) &= \frac{\mu_{\rm neq}}{2}\big(I_3^{-1/3}\mathbf{C}\cdot\mathbf{C}_{\rm v}^{-1} - 3\big) \end{aligned} \tag{16}$$

where both the equilibrium and non-equilibrium shear moduli may depend on the degree of cross-linking in the rubber (see Treloar (2005)).

On substituting(16) into (12), the following constitutive equations of the equilibrium and non-equilibrium stresses readily follow

$$\mathbf{P} = \mathbf{P}_{\rm eq} + \mathbf{P}_{\rm neq} - p\, \mathbf{F}^{-T}, \tag{17}$$

with

$$\begin{aligned} \mathbf{P}_{\rm eq} &= g_\psi(d)\, \mu_{\rm eq}\, \mathbf{F}^{-T}\mathbf{C}', \\ \mathbf{P}_{\rm neq} &= g_\psi(d)\, \mu_{\rm neq}\, \mathbf{F}^{-T}(\mathbf{C}\mathbf{C}_{\rm v}^{-1})' \end{aligned} \tag{18}$$

[1] In the rate-independent case, the dissipation density (13) simplifies to

$$\phi(d, \dot d) = G_c\,(\frac{3}{2\,\ell_f}\,\dot d + \frac{3\,\ell_f}{16}\,\nabla d\cdot\nabla \dot d),$$

which is the time derivative of the fracture energy density

$$w(d) = G_c\,(\frac{3}{2\,\ell_f}\,d + \frac{3\,\ell_f}{32}\,|\nabla d|^2).$$

This formulation corresponds to the first-order Ambrosio-Tortorelli (AT1) model (Ambrosio and Tortorelli, 1990), characterized by the linear dependence of the first term on the damage variable d. A distinctive feature of the AT1 model is that it predicts an initial purely elastic phase before the onset of fracture.

Table 1
Summary of the modeling equations for Neo-Hookean elastic energies and quadratic dissipation functions.

Balance of linear momentum (equilibrium equation)
$\mathrm{Div}\mathbf{P} + \mathbf{b} = \mathbf{0}$ in Ω_0, $\quad \mathbf{P}\mathbf{n} = \mathbf{t}$ on $\partial\Omega_0^t$
$\mathbf{P} = \mathbf{P}_{\rm eq} + \mathbf{P}_{\rm neq} - p\,\mathbf{F}^{-T}$, $\quad \mathbf{P}_{\rm eq} = (1-d)^2\,\mu_{\rm eq}\,\mathbf{F}^{-T}\mathbf{C}'$, $\mathbf{P}_{\rm neq} = (1-d)^2\,\mu_{\rm neq}\,\mathbf{F}^{-T}(\mathbf{C}\mathbf{C}_{\rm v}^{-1})'$
Evolution of viscous deformation
$\dot{\mathbf{C}}_{\rm v} = \frac{1}{\tau_{\rm v}}\Big(\mathbf{C} - \frac{1}{3}(\mathbf{C}\cdot\mathbf{C}_{\rm v}^{-1})\mathbf{C}_{\rm v}\Big)$, $\quad \mathbf{C}_{\rm v} = \mathbf{I}$ at $t = 0$
Evolution of damage variable
$\dot d = \frac{1}{\tau_{\rm d}}\Big\langle \frac{\ell_f^2}{8}\Delta d + \frac{4\ell_f\mu_{\rm eq}}{3G_c}(1-d)\Big((\mathbf{C}\cdot\mathbf{I} - 3) + \frac{\mu_{\rm neq}}{\mu_{\rm eq}}(\mathbf{C}\cdot\mathbf{C}_{\rm v}^{-1} - 3)\Big) - 1\Big\rangle$
$d = 0$ at $t = 0$ and $\nabla d\cdot\mathbf{n} = 0$ on $\partial\Omega_0$

where the $'$ indicates the deviatoric part of the tensor.

For what concerns the viscous dissipation potential $\phi_{\rm v}$, we follow a common approach in the literature (Reese and Govindjee, 1998; Sadik and Yavari, 2023; Kumar and Lopez-Pamies, 2016; Ciambella et al., 2024) by assuming $\phi_{\rm v}$ to be a quadratic isotropic function of the viscous stretch rate $\dot{\mathbf{C}}_{\rm v}$. To establish consistency with the definition of the non-equilibrium energy (16), and account for the fact that $\mathbf{C}_{\rm v}$ is a unimodular tensor, we stipulate the dissipation to be

$$\phi_{\rm v}(\dot{\mathbf{C}}_{\rm v}) = \mathbb{D}[\dot{\mathbf{C}}_{\rm v}]\cdot\dot{\mathbf{C}}_{\rm v}, \qquad \mathbb{D}[\cdot] = \frac{\eta}{4}\,(\mathbf{C}_{\rm v}^{-1}\boxtimes\mathbf{C}_{\rm v}^{-1})[\cdot], \tag{19}$$

where $\boxtimes$ is the operator $(\mathbf{A}\boxtimes\mathbf{B})\mathbf{C} = \frac{1}{2}(\mathbf{A}\mathbf{C}\mathbf{B}^T + \mathbf{A}\mathbf{C}^T\mathbf{B}^T)$ (see Ciambella et al. (2024)). The constitutive coefficient η quantifies the material's viscosity, reflecting its resistance to flow. While many elastomer theories consider η to be strain- or strain-rate-dependent, we adopt a constant viscosity approach following (Reese and Govindjee, 1998). This simplification aims to minimize the number of constitutive parameters and evaluate the overall capabilities of the proposed model.

With the definitions (18) and (19), the evolution equation of the viscous strain (15) gives

$$\tau_{\rm v}\, g_\phi(d)\, \mathbf{C}_{\rm v}^{-1}\dot{\mathbf{C}}_{\rm v}\mathbf{C}_{\rm v}^{-1} - g_\psi(d)\, \mathbf{C}_{\rm v}^{-1}\mathbf{C}\mathbf{C}_{\rm v}^{-1} - 2\,\tilde q\,\mathbf{C}_{\rm v}^{-1} = \mathbf{0} \tag{20}$$

where $\tau_{\rm v} = \eta/\mu_{\rm neq}$ is the characteristic time of bulk viscosity, and $\tilde q = q/\mu_{\rm neq}$. The Lagrangean multiplier $\tilde q$ is determined by imposing that the evolution equation satisfies $\dot{\mathbf{C}}_{\rm v}\cdot\mathbf{C}_{\rm v}^{-1} = 0$ necessary to guarantee that $\mathbf{C}_{\rm v}$ stays unimodular. As such one obtains $\tilde q = -g_\psi(d)(\mathbf{C}\cdot\mathbf{C}_{\rm v}^{-1})/6$, that together with (20) gives

$$\dot{\mathbf{C}}_{\rm v} = \frac{g_\psi(d)}{\tau_{\rm v}\, g_\phi(d)}\Big(\mathbf{C} - \frac{1}{3}(\mathbf{C}\cdot\mathbf{C}_{\rm v}^{-1})\mathbf{C}_{\rm v}\Big).$$

For simplicity, we assume that damage affects the free energy and the dissipation potential at the same rate, i.e., $g_\psi = g_\phi$. This simplification allows us to maintain a concise model formulation and, for the viscoelastic component, recover the evolution equation used in previous works on viscoelastic solids (Reese and Govindjee, 1998; Kumar and Lopez-Pamies, 2016; Ciambella et al., 2024). However, future investigations could explore more complex relationships between damage and the degradation of energy and dissipation.

The equation governing the equilibrium of the problem with the aforementioned constitutive assumptions are listed in Table 1.

4. Preliminary assessment of the model behavior

In this section, the basic predictive characteristics of the proposed model are evaluated by solving the one-dimensional problem of a tensile bar with its left-end fixed and the righ-end subjected to a time-varying displacement $\bar u(t) = \ell\,(\exp(\dot\varepsilon_0\, t) - 1)$, that leads to a constant stretch rate $\dot\varepsilon_0$. Additionally, the condition $d = 0$ is assigned at the bar endpoints to force fracture to develop in the central part of the bar. The evolution equations, and the balance equation in Table 1 specialized to the simple tension problem reduce to scalar equations in the unknown

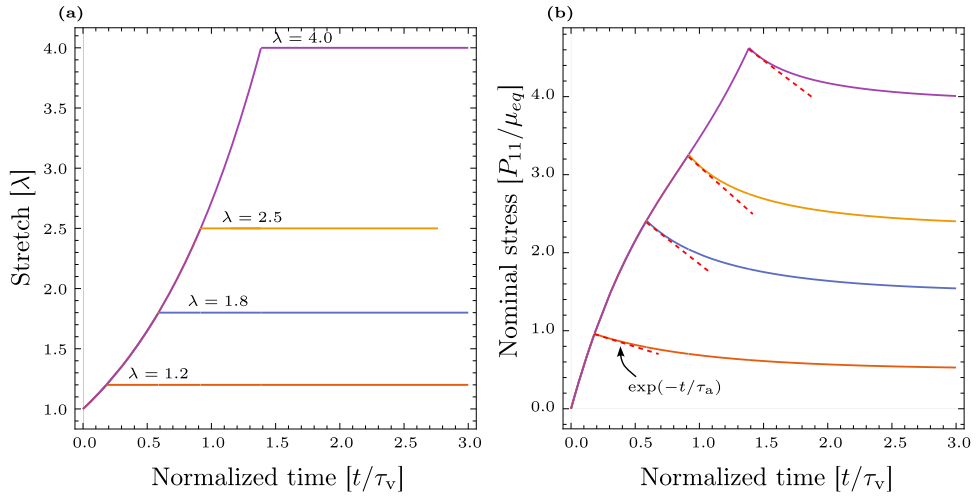

Fig. 4. Results of the 1D relaxation test at various stretch levels. (a) Applied stretch vs. normalized time (t/τ_v). (b) Nominal stress vs. normalized time, demonstrating the stress relaxation behavior. The dashed lines represent the fitting of the initial part of the stress-time curves with an exponential function.

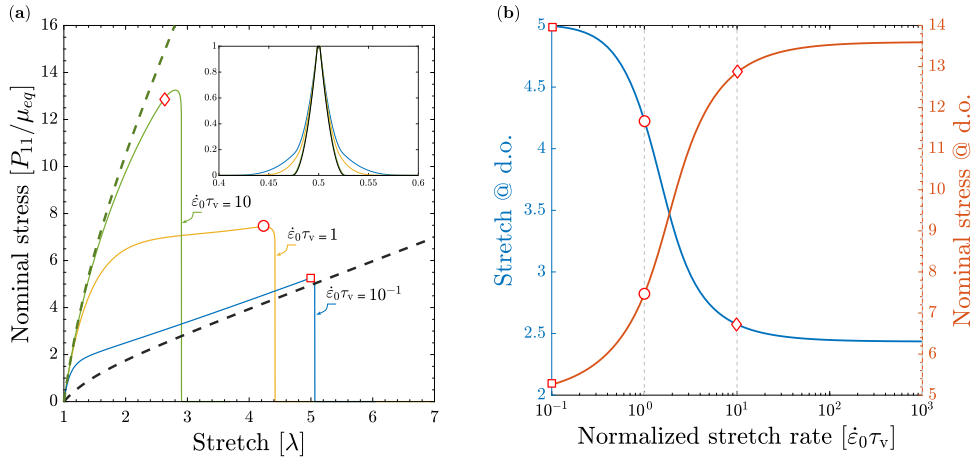

Fig. 5. Results from 1D simulations of the rupture test. (a) Plot illustrating the nominal stress versus stretch curve for various (normalized) stretch rates ($\dot{\varepsilon}_0\tau_v = \{0.1, 1, 10\}$). (b) Stretch (left axis) and Nominal stress (normalized with μ_{eq}) (right axis) at the onset of damage. The markers in (b) represent the condition at damage onset for the three curves in (a). The dashed lines in (a) represent the limiting elastic behavior of the model transitioning from the soft modulus μ_{eq} to the hard modulus $\mu_{eq} + \mu_{neq}$. The inset shows the damage profiles at complete rupture vs the damage profile of the elastic brittle fracture model (black line).

longitudinal displacement rate u, phase-field variable d and longitudinal viscous strain C_v. These equations are solved numerically, and the main results are collected in Figs. 4 and 5.

To assess the impact of the viscosity, relaxation tests were conducted by stretching samples to specific displacement level $\bar{u}$ and maintaining that displacement constant over time. Damage initiation was prevented by setting a sufficiently high fracture toughness, whereas it was set $\mu_{neq}/\mu_{eq} = 1$. The results in Fig. 4 displays the typical behavior of stress relaxation under constant stretch level. The nonlinearities in the evolution equation of $\mathbf{C}_v$ are apparent from Fig. 4(b), where, in fact, apparent relaxation time τ_a changes with the stretch level.

Additionally, rupture properties of the model were investigated by deforming the specimen at constant stretch rate until complete fracture ($d = 1$). The constitutive parameters were set to $\mu_{neq}/\mu_{eq} = 5$, $\tau_v/\tau_d = 10$, and $G_c/(\ell_f \mu_{eq}) = 15$. To localize damage at the center of the bar, a 1% reduction in tensile modulus was introduced at this point. The model exhibits clear rate-dependent behavior, as shown in Fig. 5. For increasing stretch rates, the stress–stretch curves display steeper slopes and lower ultimate stretches, consistent with experimental observations in many elastomers under high strain rates (Persson et al., 2024); the two limiting elastic behaviors are represented by dashed curves, which nearly overlap at stretch rates of $\dot{\varepsilon}_0\tau_v = 0.1$ and 10. The first limit corresponds to quasi-static loading, where only the equilibrium spring of the rheological equivalent model of Fig. 3 deforms. The second limit occurs at high loading rates, where insufficient time for dashpot relaxation causes both springs to deform in parallel. Under these conditions, both the stretch and stress at damage onset remain constant, agreeing with experimental observations in certain synthetic elastomers (Wang et al., 2017).

The inset in Fig. 5(a) compares damage profiles for three cases ($\dot{\varepsilon}_0\tau_v = \{0.1, 1, 10\}$) with the optimal damage profile from the elastic brittle fracture model. Material and damage viscosities cause a slight spreading of the damage region, most noticeable at lower stretch rates. At the highest rate ($\dot{\varepsilon}_0\tau_v = 10$), the damage profile nearly matches that of the brittle model, with a damage region of size ℓ_f.

5. Fracture of viscoelastic membranes

5.1. Governing equations for the 2D problem

In this section, we apply the proposed model to simulate the two experimental configurations commonly used to study fracture in elastomeric membranes and sketched in Fig. 1: relaxed sample cutting and pre-notched specimens.

To simulate these setups, we consider a plate-like body whose reference configuration Ω_0 is defined by a triad of orthonormal vectors, with $\mathbf{e}_1$ and $\mathbf{e}_2$ as in-plane unit vectors, and $\mathbf{e}_3$ pointing through the thickness direction. Accordingly, we set

$$\Omega_0 = \big\{ X \ : \ X = X_1\,\mathbf{e}_1 + X_2\,\mathbf{e}_2 + X_3\,\mathbf{e}_3,\ (X_1, X_2) \in [0, b] \times [0, h]\,, \quad X_3 \in [0, w] \big\}\,,$$

where the thickness is assumed to be much less than the in-plane dimensions, i.e., $w \ll \sqrt{b\,h}$.

The membrane is subjected to in-plane loading on its edges with the top and bottom faces unloaded. In this setting the problem can be studied as a two dimensional problem in which $\mathbf{u}(X_1, X_2, t)$ represents the average displacement, such that $\mathbf{u} \cdot \mathbf{e}_3 = 0$ (Lancioni and Royer-Carfagni, 2009). The macroscopic deformation $\mathbf{C}$ depends only on the in-plane variables (X_1, X_2) and takes the form

$$\mathbf{C} = c_1\,\mathbf{e}_1 \otimes \mathbf{e}_2 + c_2\,\mathbf{e}_2 \otimes \mathbf{e}_2 + c_3\,\mathbf{e}_3 \otimes \mathbf{e}_3 + c_{12}\,(\mathbf{e}_1 \otimes \mathbf{e}_2 + \mathbf{e}_2 \otimes \mathbf{e}_1)\,,$$

where the dependence on position and time has been omitted for brevity. The out-of-plane component c_3 is used to maintain an isochoric deformation, by requiring that

$$c_3 = (c_1 c_2 - c_{12}^2)^{-1}, \tag{21}$$

while the conditions

$$c_1 > 0,\ c_2 > 0, \quad \text{and} \quad c_{12}^2 < c_1 c_2 \tag{22}$$

ensure that $\mathbf{C}$ is a positive definite tensor.

The viscous deformation $\mathbf{C}_{\rm v}$ is postulated in the same form

$$\mathbf{C}_{\rm v} = c_{v_1}\,\mathbf{e}_1 \otimes \mathbf{e}_2 + c_{v_2}\,\mathbf{e}_2 \otimes \mathbf{e}_2 + c_{v_3}\,\mathbf{e}_3 \otimes \mathbf{e}_3 + c_{v_{12}}\,(\mathbf{e}_1 \otimes \mathbf{e}_2 + \mathbf{e}_2 \otimes \mathbf{e}_1)\,.$$

with c_{v_1}, c_{v_2}, $c_{v_{12}}$ and c_{v_3} satisfying the same conditions in Eqs. (21) and (22).

The damage is assumed uniform through the cross-section, such that $d = d(X_1, X_2)$ and the Laplacian in (14) is evaluated only in terms of these two variables.

Due to the negligible thickness of the plate, we assume a state of plane stress, i.e., $\mathbf{P}\mathbf{e}_3 \cdot \mathbf{e}_3 = 0$. This allows us to express the reactive pressure term p in Eq. (17) in terms of equilibrium (independent of $\mathbf{C}_{\rm v}$) and non-equilibrium components:

$$p_{\rm eq} = g_\psi\,\mu_{\rm eq}\,\Big(c_3 - \frac{1}{3}(c_1 + c_2 + c_3)\Big)\,,$$

$$p_{\rm neq} = \frac{1}{3} g_\psi\,\mu_{\rm neq}\,(2\,c_2\,c_3\,c_{v_1} - c_2(c_1 + c_{v_1})\,c_{v_3} + 2\,c_{v_{12}}(c_{12}c_{v_3} - c_3 c_{v_{12}}))\,,$$

such that $p = p_{\rm eq} + p_{\rm neq}$. Substituting this into Eq. (17) yields the expression of the Piola–Kirchhoff stress tensor.

The evolution problem of the inelastic variables $\mathbf{C}_{\rm v}$ and d can be recast in dimensionless form by introducing dimensionless space $\tilde{X} = X/\ell_f$ and time $\tilde{t} = t/\tau_d$ variables, to obtain

$$\begin{aligned} \dot{\mathbf{C}}_{\rm v} &= \frac{1}{\tau}(\mathbf{C} - \frac{1}{3}(\mathbf{C} \cdot \mathbf{C}_{\rm v}^{-1})\mathbf{C}_{\rm v}), \\ \dot{d} &= \Big\langle \frac{1}{8}\,\Delta d + \frac{4}{3\chi}(1-d)\,((\mathbf{C}\cdot\mathbf{I} - 3) + \beta\,(\mathbf{C}\cdot\mathbf{C}_{\rm v}^{-1} - 3)) - 1 \Big\rangle\,. \end{aligned} \tag{23}$$

where, with an abuse of notation, the same symbols are used to denote derivatives with respect to the dimensionless variables. Eq. (23) shows that the evolution problem is determined by only three constitutive parameters

$$\tau = \frac{\tau_{\rm v}}{\tau_{\rm d}}, \qquad \chi = \frac{G_c}{\ell_f\,\mu_{\rm eq}}, \qquad \beta = \frac{\mu_{\rm neq}}{\mu_{\rm eq}}\,.$$

The influence of these parameters on fracture propagation is analyzed in the next subsection with reference to the two type of experiments discussed above.

5.2. Relaxed sample cutting

In the relaxed sample cutting configuration (Chen et al., 2011; Mai et al., 2020; Corre et al., 2020), the experimental procedure is sketched in Fig. 1(a)–(c) and comprises three phases:

(a) **Quasi-static loading phase**. The intact specimen is subjected to quasi-static stretching until reaching a prescribed stretch λ_{pre}. During this phase, the viscous deformation tensor equals the total deformation tensor, $\mathbf{C}_{\rm v} = \mathbf{C}$, and both the non-equilibrium free energy density and non-equilibrium component of the first Piola–Kirchhoff stress vanish ($\psi_{\rm neq} = 0$ and $\mathbf{P}_{\rm neq} = \mathbf{0}$). This indicates that the specimen is in its relaxed state, with stress solely attributed to the equilibrium component, $\mathbf{P}_{\rm eq}$. Numerically, this is achieved by excluding viscous iterations from the algorithm detailed in Appendix.

(b) **Crack initiation phase**. A damaged region representing a cut is introduced into the pre-stretched specimen. This process is assumed instantaneous relative to the model's characteristic timescales, meaning $\mathbf{C}_{\rm v}$ remains unchanged from the end of the initial phase. Non-equilibrium stresses $\mathbf{P}_{\rm neq}$ develop near the crack tip, while the rest of the specimen remains in equilibrium. An incremental numerical procedure progressively increases the damage variable within the cut region from 0 to 1, updating the displacement field accordingly.

(c) **Crack propagation phase**. Both characteristic times $\tau_{\rm v}$ and $\tau_{\rm d}$ become relevant as the crack propagates, with the complete set of state variables $\{\mathbf{u}, \mathbf{C}_{\rm v}, d\}$ evolving.

Exploiting the symmetry of the experimental setup (Fig. 1(a)–(c)), numerical simulations are performed on a portion of the left half of the specimen (Fig. 1(f)). The computational domain has dimensions (normalized to ℓ_f) of $b/2 = 40$ in length, $h = 100$ in height, and a unit thickness ($w = 1$). To accurately capture the fracture process, a refined mesh with an element size of 0.1 is used in a narrow vertical band near the right edge, where crack propagation is expected.

Following the initial quasi-static pre-stretching phase, a crack of length $a = 10$ is introduced at the lower end of the right edge, achieved by setting the damage variable $d = 1$ on the corresponding boundary segment. Due to the crack's propagation along the specimen's symmetry axis, only half of the band where the phase-field d localizes is represented in the computational domain.

Fracture initiates from the tip of the pre-existing crack and propagates upward along the right edge, following three distinct phases of crack speed as shown in Fig. 6 for a pre-stretch $\lambda_{pre} = 2$: an initial acceleration of the crack, followed by an intermediate steady-state phase with a constant velocity, and a final accelerating phase influenced by the boundary conditions applied at the upper end of the computational domain. All simulations carried out with different constitutive parameters have shown similar crack speed curves, with the aforementioned three phases.

Parametric analysis. The impact of the parameters τ and β on fracture propagation is here examined. The pre-stretch was set to $\lambda_{pre} = 2$ and $\chi = 15$ was kept constant in all the following simulations. Fig. 7 shows the relationship between crack speed $\dot{a}$ and τ for various values of β. The results indicate that crack speed $\dot{a}$ decreases as both τ and β increase. The maximum crack speed ($\dot{a} = 5.32$) is attained in the purely elastic scenario ($\tau = 0$ - "no viscoelasticity" in the figure) because the material lacks the ability to dissipate energy through viscoelastic mechanisms.

On the other hands, τ controls the delay in the opening of crack lips that in turn reduces the crack propagation speed. This is indeed

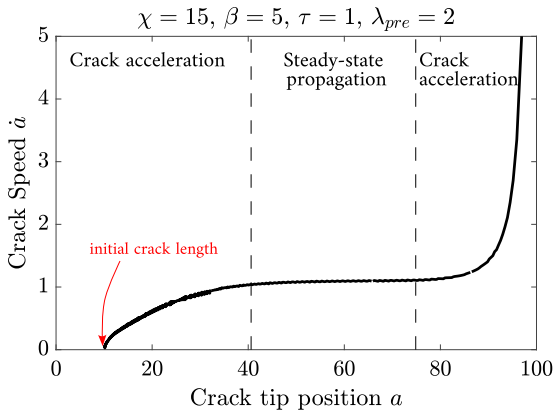

Fig. 6. Crack speed $\dot{a}$ versus crack length a with indication of the three regimes observed in the numerical simulations.

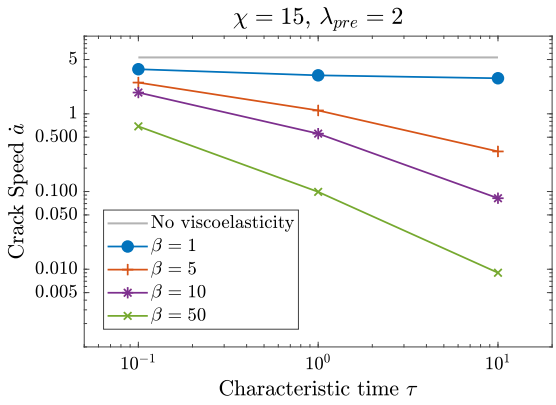

Fig. 7. Crack speed $\dot{a}$ versus characteristic time τ for different values of β.

confirmed by the amplitude of the velocity field $|\dot{\mathbf{u}}|$ shown in Fig. 8 for $\beta = 5$. As τ increases, two primary effects are observed: (i) the maximum magnitude of the velocity field, $|\dot{\mathbf{u}}|$, decreases, while the region behind the crack tip where the velocity field is non-zero expands significantly; (ii) the shape of the crack lips changes from parabolic to wedge-like, due to the time delay in opening the crack lips caused by the increased relaxation time. As τ grows, this effect becomes more pronounced, resulting in a slower crack propagation speed.

Fig. 9 shows the components $P_{\text{eq}} = \mathbf{P}_{\text{eq}} \cdot \mathbf{e}_1 \otimes \mathbf{e}_1$ and $P_{\text{neq}} = \mathbf{P}_{\text{neq}} \cdot \mathbf{e}_1 \otimes \mathbf{e}_1$ of the equilibrium and non-equilibrium Piola stress tensors, respectively, corresponding to the same time snapshots in Fig. 8. The non-equilibrium component P_{neq} has negative values in an area near the crack lip, that becomes larger as τ increases. This region experiences compressive non-equilibrium stresses, that tends to unload the dashpot in the rheological equivalent scheme initially at $\mathbf{C}_{\text{v}} = \mathbf{C}$. This in turn promotes the opening of the crack lip. Ahead of the crack tip, P_{eq} decreases while P_{neq} increases with τ, yet the total stress $P = P_{\text{eq}} + P_{\text{neq}}$ remains unchanged. These stress distributions arise from the delayed stretch increment ahead of the crack tip due to viscosity.

The influence of β is examined in Figs. 10 and 10, where the velocity $|\dot{\mathbf{u}}|$ and stresses P_{eq} and P_{neq} are plotted for different β values, with $\tau = 1$. In this scenario, β does not affect the crack profile shape or stress distribution but only reduces the velocity amplitude $|\dot{\mathbf{u}}|$ (see Fig. 10) and, consequently, the crack speed. An increase in β raises the non-equilibrium stiffness μ_{neq}, making elastic strain development more energetically costly compared to the viscous strains. Since viscous strains require time to develop, the system evolves more slowly, thereby reducing the crack propagation speed.

Tearing energy. During the crack propagation phase, no external energy is supplied to the material since the applied stretch remains constant. Consequently, the energetic cost of advancing the crack is paid for by the stored strain energy (Persson et al., 2024; Barthel, 2024). The tearing energy, i.e., the energetic cost of advancing the crack front, is defined as:

$$\Gamma = -\frac{\partial \mathcal{F}}{\partial a},$$

with $\mathcal{F}$ defined in Eq. (2).

In the steady-state regime, the specimen can be divided into three distinct regions: (i) a region ahead of the crack tip that is far enough away to experience a state of uniform pure shear, and so the definition is:

$$\mathbf{C} = \lambda_{pre}^2 \mathbf{e}_1 \otimes \mathbf{e}_1 + \mathbf{e}_2 \otimes \mathbf{e}_2 + \frac{1}{\lambda_{pre}^2} \mathbf{e}_3 \otimes \mathbf{e}_3; \tag{24}$$

(ii) a region close to the crack tip that undergoes rate-dependent non-uniform straining, and (iii) a region behind the crack tip, sufficiently remote from it, that remains undeformed.

According to this schematic representation, crack propagation can be conceptualized as the upward translation of the second region, leading to a reduction in the first region and an expansion of the third region. This mechanism follows the principle of translational invariance discussed in many previous works (Schapery, 2022; Shrimali and Lopez-Pamies, 2023c; Morishita et al., 2016), which, in the present context, is achieved whenever $h \gg b$, to ensure the presence of region (i), and $h \gg \dot{a}\tau$ to ensure the presence of the region (iii). As an additional crack length da is introduced, a volume $b \times da \times w$ of the specimen transitions from the pure shear state to the undeformed state. The tearing energy, Γ, is thus the elastic strain energy of a volume $b \times 1 \times w$ in the pure shear strain state (24), that is:

$$\Gamma = bw \frac{\mu_{\text{eq}}}{2} (\lambda_{pre}^2 + \frac{1}{\lambda_{pre}^2} - 2), \tag{25}$$

in which the same functional form in $(16)_1$ was used for the energy. This expression provides an analytical estimate of the tearing energy. Alternatively, a numerical estimate can be obtained using the relationship $\Gamma = -\dot{\mathcal{F}}/\dot{a}$. By separating viscous and fracture contributions, the tearing energy can be decomposed as sum of viscous and fracture components

$$\Gamma = \Gamma_v + \Gamma_f, \quad \text{with } \Gamma_v = \frac{\mathcal{P}_v}{\dot{a}}, \text{ and } \Gamma_f = \frac{\mathcal{P}_f}{\dot{a}},$$

and

$$\begin{aligned} \mathcal{P}_v &= \frac{\tau\beta}{2} \int_{\Omega_0} (1-d)^2 \mathbf{C}_{\text{v}}^{-1} \dot{\mathbf{C}}_{\text{v}} \cdot \dot{\mathbf{C}}_{\text{v}} \mathbf{C}_{\text{v}}^{-1}, \\ \mathcal{P}_f &= \frac{3\chi}{2} \int_{\Omega_0} (\dot{d}(1+\dot{d})) + \frac{1}{8} \nabla d \cdot \nabla \dot{d}, \end{aligned} \tag{26}$$

the viscous and fracture dissipation rates, obtained from the dimensionless forms of the constitutive Eqs. (13) and (19). The dissipation rates (26) differ from the dissipation potential (13) for the viscous terms which are twice those in (13).

Fig. 12 illustrates the tearing energy components (Γ, Γ_v, Γ_f) as functions of the dimensionless characteristic time τ and coefficient β, for fixed $\chi = 15$ and pre-stretch level $\lambda_{pre} = 2$.

In Fig. 12(a), with a constant pre-stretch level, the total tearing energy Γ remains nearly constant and close to the theoretical value predicted by (25). This is expected due to the consistent amount of stored strain energy available for crack propagation under constant pre-stretch conditions. However, the components Γ_v and Γ_f vary significantly with τ and β. Notably, increasing either τ or β leads to a decrease in Γ_f and a corresponding increase in Γ_v.

Fig. 12(b) further demonstrates a direct proportionality between Γ_f and crack propagation speed $\dot{a}$, and an inverse proportionality between Γ_v and $\dot{a}$ within the examined parameter range. This indicates that the energy available for crack opening Γ_f directly influences the crack

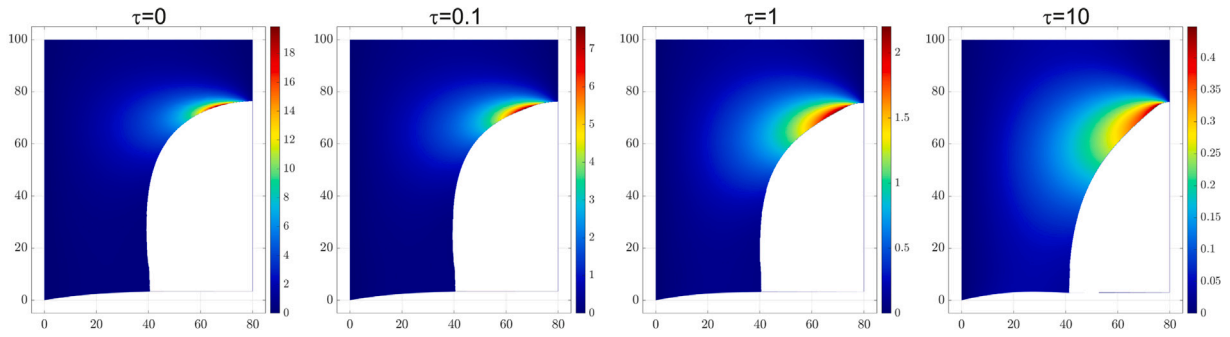

Fig. 8. Velocity amplitude $|\dot{\mathbf{u}}|$ for different values of τ, at fixed $\chi = 15$, $\beta = 5$ and $\lambda_{pre} = 2$.

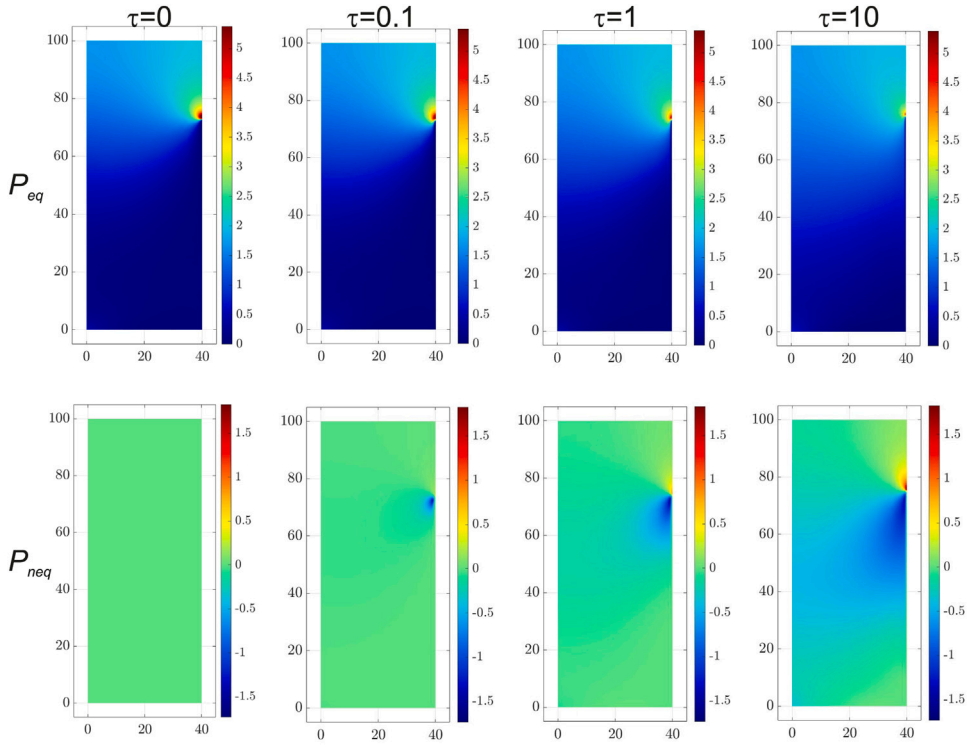

Fig. 9. Components P_{eq} and P_{neq} of the equilibrium and non-equilibrium Piola stress tensors for different values of τ, at fixed $\chi = 15$, $\beta = 5$ and $\lambda_{pre} = 2$.

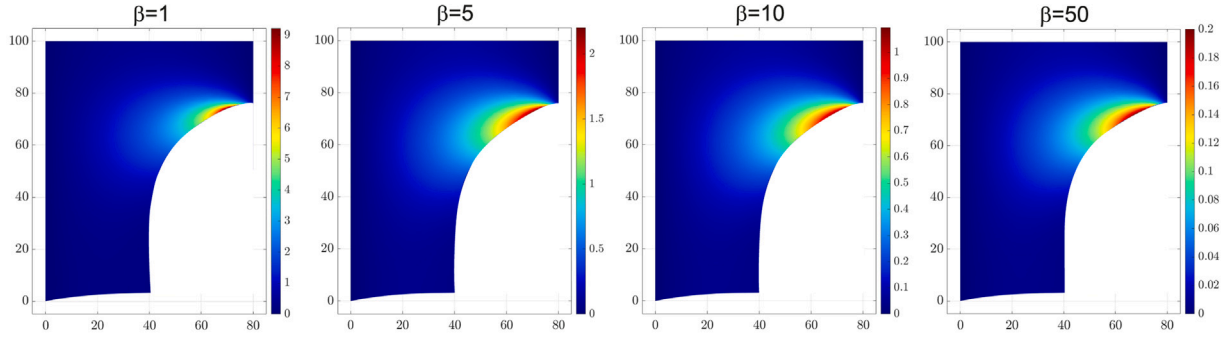

Fig. 10. Velocity amplitude $|\dot{\mathbf{u}}|$ for different values of β, at fixed $\chi = 15$, $\tau = 1$ and $\lambda_{pre} = 2$.

speed, while the energy dissipated through viscous effects Γ_v hinders crack propagation. This shift suggests that increased viscoelastic effects through β or τ hinder the material's ability to efficiently convert stored elastic energy into fracture energy, resulting in a lower crack propagation speed $\dot{a}$.

Simulations at different pre-stretch levels λ_{pre}. The influence of pre-stretch λ_{pre} on fracture propagation is examined by varying λ_{pre} from 1.5 to 3.5. Consistent with experimental results (Corre et al., 2020), it is observed that crack speed increases with increasing pre-stretch, as depicted by the curves of $\dot{a}$ as a function of λ_{pre} and Γ in . The blue

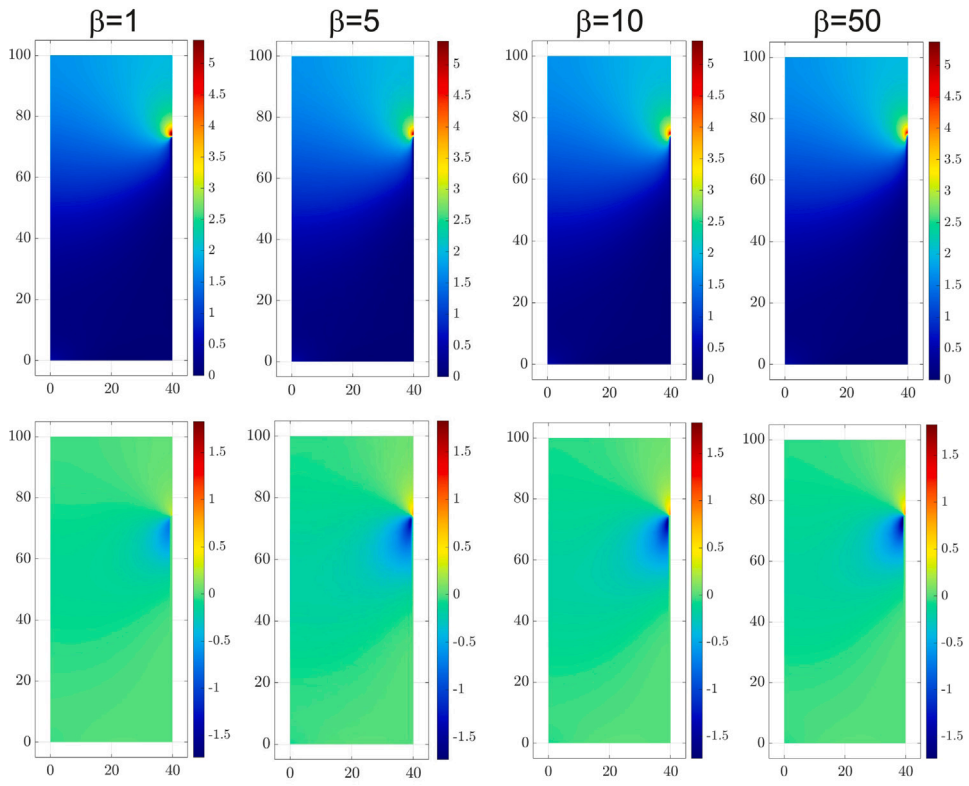

Fig. 11. Transversal components P_{eq} and P_{neq} of equilibrium and non-equilibrium Piola stress tensors for different values of β, at fixed $\chi = 15$, $\tau = 1$ and $\lambda_{pre} = 2$.

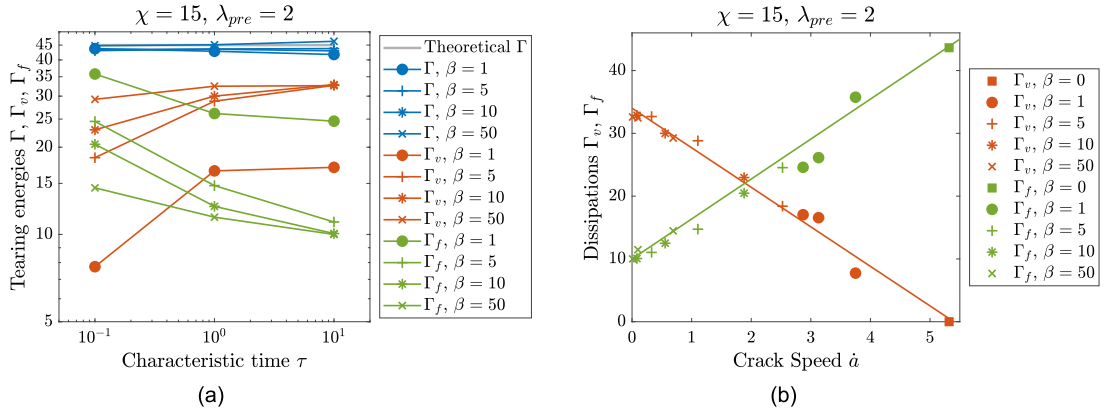

Fig. 12. (a) Tearing energy Γ (blue line), with its viscous part Γ_v (orange line) and fracture part Γ_f (green line), as function of τ for different values of β. (b) Γ_v and Γ_f as functions of the crack speed $\dot{a}$. (For interpretation of the references to color in this figure legend, the reader is referred to the web version of this article.)

curves represent numerical simulations for different pairs of (β, τ) values, with $\chi = 15$ held constant. These numerical results are compared with experimental data (yellow line) from Mai et al. (2021) reported in Fig. 2, showing close agreement with the high-velocity branches and capturing the power-law relationship between $\dot{a}$ and λ_{pre}, as well as between $\dot{a}$ and Γ, seen in the experiments (Mai et al., 2020, 2021; Morishita et al., 2016).

The simulations also replicate the change in crack profile shape from parabolic to wedge-like as observed in the experiments of Morishita et al. (2016), Corre et al. (2020), Mai et al. (2020). Fig. 14 illustrates this transformation, accompanied by an expansion of the high-velocity amplitude region $|\dot{\mathbf{u}}|$ behind the crack tip. The increase in stored strain energy with λ_{pre} results in a corresponding rise in the tearing energy Γ, as well as its components Γ_v and Γ_f, as shown in Fig. 15.

The distributions of non-equilibrium strain energy Ψ_{neq} and stress P_{neq} for varying λ_{pre} are analyzed in Fig. 16, normalized as:

$$\hat{\Psi}_{\text{neq}} = \frac{\Psi_{\text{neq}}}{\Psi_{pre}}, \quad \hat{P}_{\text{neq}} = \frac{P_{\text{neq}}}{P_{pre}},$$

where $\Psi_{pre} = \frac{1}{2}\left(\lambda_{pre}^2 + \frac{1}{\lambda_{pre}^2} - 2\right)$ is the strain energy density, and $P_{pre} = \frac{d\Psi_{pre}}{d\lambda_{pre}} = \lambda_{pre} - \frac{1}{\lambda_{pre}^3}$ is the normal stress component in the pure-shear strain state at the end of the pre-stretching phase.

As λ_{pre} increases, the contour plots in Fig. 16 show an expansion of the region near the crack tip where the density $\hat{\Psi}_{neq}$ localizes. In this zone, $\hat{P}_{neq}$ attains negative values behind the crack tip, indicating strain relaxation towards the unstrained state, and positive values ahead of

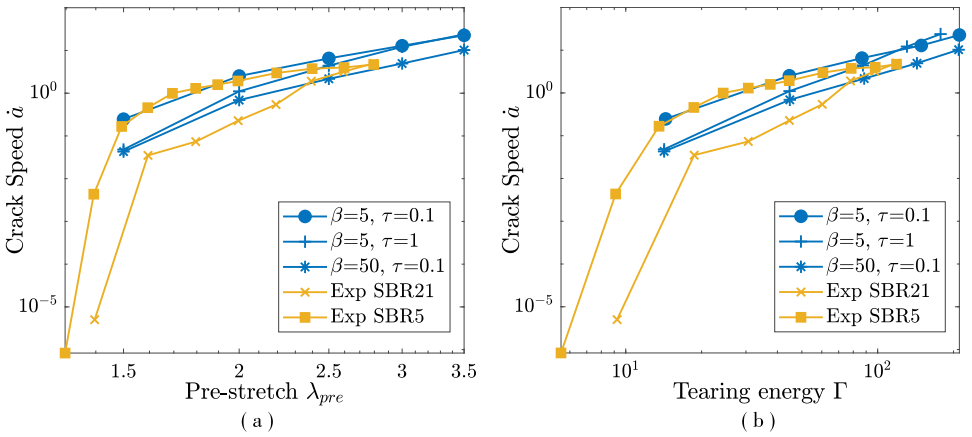

Fig. 13. Crack speed $\dot{a}$ at different values of (a) pre-stretch λ_{pre} and (b) tearing energy Γ. The blue curves are numerical and they correspond to three different sets of parameters. The yellow curves are obtained from the experiments reported in Mai et al. (2021) on two different elastomers. (For interpretation of the references to color in this figure legend, the reader is referred to the web version of this article.)

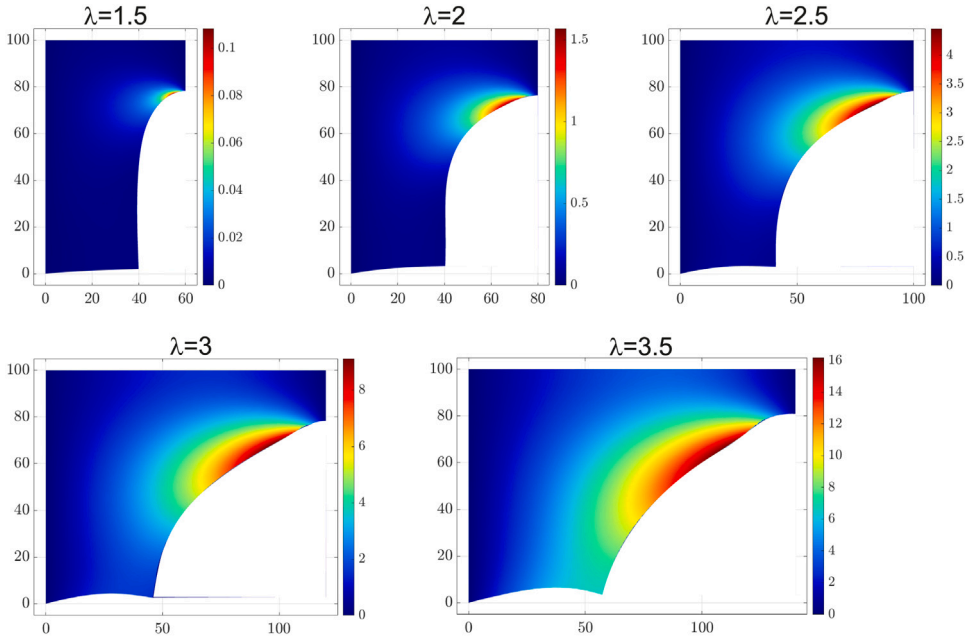

Fig. 14. Velocity amplitude $|\dot{\mathbf{u}}|$ for different values of λ_{pre}, at fixed $\chi = 15$, $\beta = 50$ and $\tau = 0.1$.

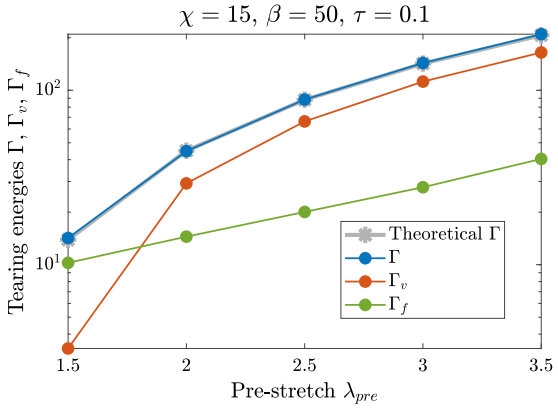

Fig. 15. Tearing energy Γ (blue line) and its two components Γ_v (orange line) Γ_f (green line) at different values of the pre-stretch λ_{pre}. The theoretical Γ values (gray asterisks) overlap with the numerical Γ values (blue dots). (For interpretation of the references to color in this figure legend, the reader is referred to the web version of this article.)

the crack tip, indicating increasing strains due to the imminent fracture. The increase in λ_{pre} not only enhances the crack speed but also reduces the time available for material strain relaxation, thereby enlarging the non-equilibrium zone where rate-dependent strains develop.

Additionally, for lower pre-stretch values ($\lambda_{pre} = 1.5, 2$), $\hat{\Psi}_{neq}$ is nearly zero in the region ahead of the crack tip, and $\hat{P}_{neq}$ shows minimal positive values, suggesting the material remains in a rubbery state. However, as λ_{pre} increases, both $\hat{\Psi}_{neq}$ and $\hat{P}_{neq}$ increase significantly ahead of the crack tip, indicating a transition from a soft to a hard solid state. This transition for increasing λ_{pre} is analogous to observations in previous studies (Kubo and Umeno, 2017; Kubo et al., 2021), explaining the transition from low-speed to high-speed crack propagation.

5.3. Stretching of pre-notched specimen

We simulate the failure process of notched membranes stretched at a constant velocity. The test's geometric setup is depicted in Figs. 1(d, e). The dimensions of the computational domain and the mesh

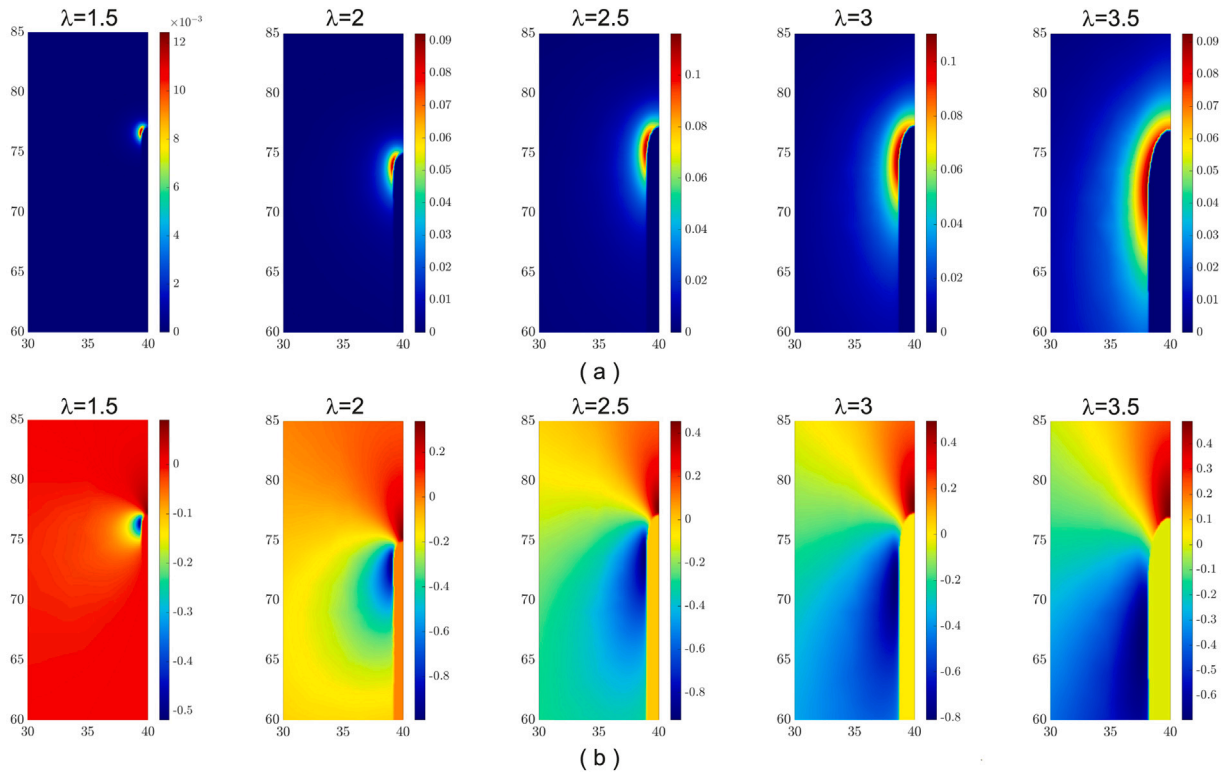

Fig. 16. (a) Normalized non-equilibrium energy density $\hat{\Psi}_{neq}$, and (b) normalized component $\hat{P}_{neq}$ of non-equilibrium Piola stress tensor for different values of λ_{pre}, at fixed $\chi = 15$, $\beta = 50$ and $\tau = 0.1$. Plots are restricted to a rectangular region 10×25 around the crack tip.

discretization are the same of previous section, whereas a pre-crack of length $a = 10$ is introduced at the bottom of the right edge of the computational domain (Fig. 1(d)). The specimen is loaded by applying a constant-rate horizontal displacement $\bar{u}(t) = b\,\dot{\lambda}\,t$ at the right edge while fixing the left edge. The loading rate $\dot{\lambda}$ defines a characteristic timescale $\tau_\lambda = \dot{\lambda}^{-1}$ that interacts with both material and damage viscosity timescales. Using fixed constitutive parameters $\chi = 15$ and $\beta = 5$, simulations are performed at two distinct characteristic times, $\tau = 0.1$ and $\tau = 100$, while varying $\dot{\lambda}$. For $\tau = 0.1$ ($\tau_v < \tau_d$), the triplet of dimensionless parameters (τ, χ, β) matches the one used in Section 5.2 to study crack speed at different pre-stretches. With these parameters, the simulations showed satisfactory agreement with the experimental results (see). The parameter τ was also set to $\tau = 100$ to explore the scenario where $\tau_v > \tau_d$. This provides insights into how the interaction between the timescales of loading (τ_λ), material viscosity (τ_v), and damage viscosity (τ_d) influences the membrane's mechanical response.

Simulations for $\tau = 0.1$. In these simulations, $\dot{\lambda}$ varies from 0.001 to 0.1 ($\tau_\lambda \in [10, 1000]$), and the condition $\tau_v < \tau_d < \tau_\lambda$ is maintained throughout the analysis.

Fig. 17 shows the nominal stress–stretch curves for various $\dot{\lambda}$ values. The average nominal stress $\bar{P}$ is defined as $\bar{P} = F/(hw)$, where F is the normal reactive force on the left edge, h is the specimen height, and w is its thickness. Since τ_λ exceeds both τ_v and τ_d, both material and damage viscosities fully develop during deformation. The material stretches in a rubbery state with negligible non-equilibrium stresses. The curves differ in their final concave branches, where slopes gradually decrease to negative values over stretch ranges that widen with increasing $\dot{\lambda}$. These branches represent crack propagation, which initiates at λ_{onset} and proceeds slowly relative to the stretching rate due to micro-viscosity effects.

Notably, the curves in Fig. 17 qualitatively match tensile experiments on double-edge notched specimens of polyurethane elastomers

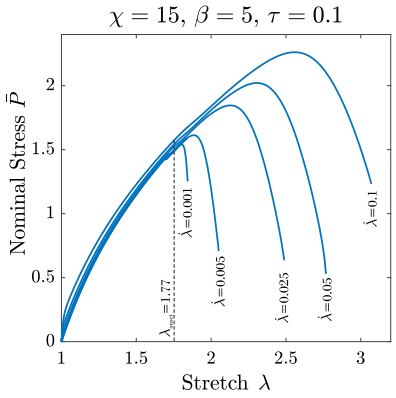

Fig. 17. Simulations for $\tau = 0.1$. Nominal stress $\bar{P}$ versus stretch λ for different stretch rates $\dot{\lambda}$.

reported in Cristiano et al. (2011) (Fig. 8 therein) as well as single-edge notched specimens studied in Kamarei et al. (2024).

Simulations for $\tau = 100$. Fig. 18(a) displays stress–stretch curves for different $\dot{\lambda}$ values. Fig. 18(b) shows the power contributions at the onset of failure (corresponding to peak points of the $\bar{P} - \lambda$ curves) plotted against $\dot{\lambda}$. Three components are shown: elastic power $\mathcal{P}_{ela} = \int_{\Omega_0} \Psi$ (solid line), viscous dissipation rate $\mathcal{P}_v$ (dotted line), and fracture dissipation rate $\mathcal{P}_f$ (dashed line), as defined in (26). Each component is normalized by the external power $\mathcal{P}_{ext} = bF\dot{\lambda}$. Analysis of Fig. 18 reveals three distinct regimes:

i *Low-speed regime* ($\dot{\lambda} < 0.002$, i.e., $\tau_\lambda > 500$): When $\tau_d < \tau_v \ll \tau_\lambda$, the slow loading allows full development of viscous strains that closely match total strain, minimizing non-equilibrium elastic strain energy. The ochre curve in Fig. 18(a) shows initial hard

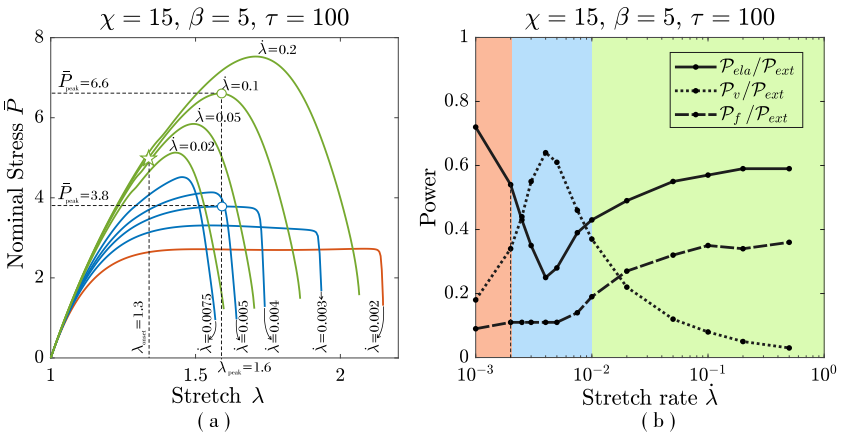

Fig. 18. Simulations for $\tau = 100$. (a) Nominal stress $\bar{P}$ versus stretch λ for different stretch rates $\dot{\lambda}$. (b) Elastic power $\mathcal{P}_{ela}$ and viscous and fracture dissipation rates $\mathcal{P}_v$ and $\mathcal{P}_f$ at fracture onset for different values of $\dot{\lambda}$.

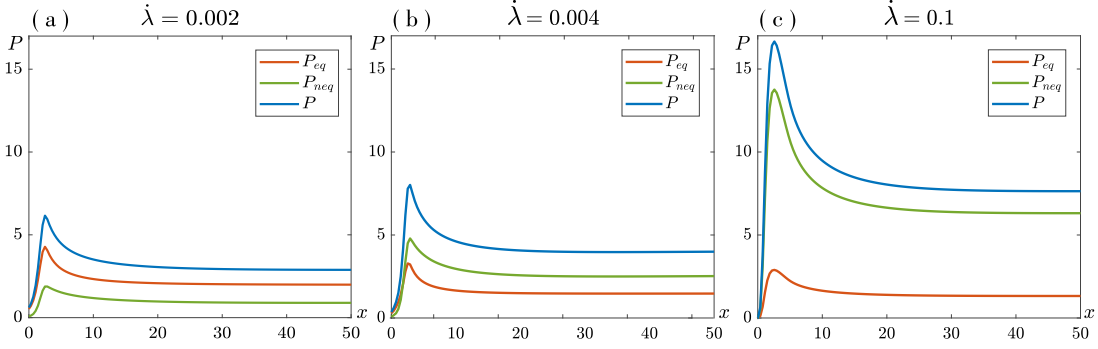

Fig. 19. Simulations for $\tau = 100$. Stresses components P, P_{eq} and P_{neq} on a line ahead of the crack tip at fracture onset.

material modulus ($\mu_{eq} + \mu_{neq}$) transitioning to soft behavior (μ_{eq}), followed by crack propagation softening. In Fig. 18(b), the ochre-shaded region shows low dissipation rates but high elastic power at fracture onset.

ii *Intermediate-speed regime* ($0.002 < \dot{\lambda} < 0.01$, $100 < \tau_\lambda < 500$): Here, τ_λ is comparable to τ_v, allowing only partial viscous strain development. This produces steeper stress–stretch curves (blue curves in Fig. 18(a)) indicating enhanced non-equilibrium stiffness. The blue-shaded region in Fig. 18(b) shows increased viscous dissipation at the expense of elastic power due to ongoing viscous stretching.

iii *High-speed regime* ($\dot{\lambda} > 0.01$, $\tau_\lambda < 100$): When $\tau_\lambda < \tau_v$, insufficient time for viscous strain development results in primarily elastic strains and hard material state. The green curves in Fig. 18(a) overlap initially but diverge in later stages with different peak stresses and softening behaviors. Fracture yielding condition $(23)_2$ (with $\dot{d} = 0$) occurs at $\lambda_{onset} \simeq 1.3$ (star-marked point). Beyond this point, crack propagation is initially very slow, shown by progressively bending response curves that peak and then soften. These branches widen with increasing rate of deformation. The curves in this regime share similarities with the curves in Fig. 17 for $\tau = 0.1$. In both cases, crack propagation is dominated by damage viscosity, being τ_λ close to τ_d. However, they differ significantly in stress levels. The green curves in Fig. 18(a) exhibit higher stresses due to hard material state ($\tau_v > \tau_\lambda$), while the curves of Fig. 17 shows lower stresses due to soft material state ($\tau_v \ll \tau_\lambda$).

The green-shaded region in Fig. 18(b) shows reduced viscous dissipation but increased fracture dissipation due to greater crack-tip viscous dissipation.

Analysis of the peak points in the stress–strain curves (Fig. 18(a)) reveals distinct trends in the peak stress $\bar{P}_{peak}$ and peak strain λ_{peak} with varying stretch rates. While $\bar{P}_{peak}$ consistently increases with $\dot{\lambda}$, the behavior of λ_{peak} is more complex: it decreases at low and intermediate $\dot{\lambda}$ values but increases at high $\dot{\lambda}$. For stretch rates in the range $\dot{\lambda} \in [0.004, 0.1]$, $\bar{P}_{peak}$ nearly doubles from 3.8 to 6.6, whereas λ_{peak} remains relatively constant at 1.6. This rate-independent peak stretch behavior aligns with experimental observations reported in Pharr et al. (2012), Wang et al. (2017) and further validated in Shrimali and Lopez-Pamies (2023b), where the critical stretch (peak stretch) shows no significant dependence on the stretch rate.

Fig. 19 shows the tensile stress distribution along a vertical line ahead of the crack tip at the peak stretch λ_{peak} obtained from three simulations with stretch rates $\dot{\lambda} = 0.002$, 0.004 and 0.1, which are representative of previously mentioned regimes. Profiles of the transverse component of the Piola–Kirchhoff stress tensor $P = \mathbf{P} \cdot (\mathbf{e}_1 \otimes \mathbf{e}_1)$, along with its equilibrium (P_{eq}) and non-equilibrium (P_{neq}) components are drawn. The profile of P increases with rising $\dot{\lambda}$, reflecting the steepening of the curves shown in Fig. 18(a). This increase is driven by the progressive growth of P_{neq}, while P_{eq} remains unchanged. For $\dot{\lambda} = 0.002$, the soft material state results in very low values of P_{neq}. In contrast, for $\dot{\lambda} = 0.1$, the hard state leads to values of $P_{neq} \simeq \beta P_{eq}$.

6. Conclusions

In this paper, we have introduced a thermodynamically consistent phase-field model that incorporates a finite characteristic time for damage evolution, distinct from the characteristic time for viscous relaxation. This distinction allows us to capture the different time scales associated with bulk dissipation due to viscoelastic effects and dissipation in the fracture process zone due to chain scission and

cavitation. We adopted a modeling framework that incorporates only three constitutive parameters: β, χ, τ, that represent the ratio of the non-equilibrium to equilibrium shear moduli, the normalized fracture toughness and the ratio between viscous characteristic time $\tau_{\rm v}$ and the damage proper time $\tau_{\rm d}$, respectively. This framework facilitates the explicit decomposition of energetic and dissipative contributions during fracture propagation, enabling differentiation between dissipative mechanisms occurring at the distinct characteristic timescales $\tau_{\rm v}$ and $\tau_{\rm d}$ associated with viscous relaxation and damage evolution, respectively.

The model was validated against two distinct experimental setups: *relaxed membrane cutting* and *pre-notched membrane stretching*. Numerical tests, conducted in a dimensionless framework, revealed a broad range of phenomena arising from the interplay of the different time-depending dissipative mechanisms. The numerical predictions are primarily qualitative, without attempting to provide detailed quantitative comparisons with experiments, which are left to future studies.

i. Simulations of relaxed sample cutting (Section 5.2) demonstrated the model's ability to accurately capture two key experimental observations: 1. the variations in crack lip profiles at different crack speeds, and 2. the power-law relationships between pre-stretch levels, tearing energy, and crack speed. A key finding is the complex interaction between bulk viscoelasticity and the damage zone at the crack tip, which significantly influences crack propagation dynamics. Specifically, for certain ranges of constitutive parameters, the region behind the crack tip experiences negative non-equilibrium normal stresses that delay crack lip opening, thereby reducing propagation speed. The model also provided insights into the spatial distribution of non-equilibrium strain energy and stress near the crack tip. These distributions revealed a clear transition from rubbery (soft solid) to glassy (hard solid) behavior ahead of the crack tip with increasing pre-stretch, consistent with experimental observations.

ii. Simulations of pre-notched membrane stretching (Section 5.3) revealed the complex interplay between deformation rate and material characteristic times in both crack initiation and propagation. We identified distinct evolution regimes where the relative magnitudes of loading time τ_λ and the two timescales $\tau_{\rm v}$ and $\tau_{\rm d}$ govern the material response. It was observed that for values of τ_λ close to $\tau_{\rm v}$, viscous dissipation is maximized, and the critical stretch at fracture onset shows only a very slight dependence on the stretch rate, unlike the critical stress, which varies significantly. These numerical predictions align with the experimental findings reported in Pharr et al. (2012), Wang et al. (2017), where a rate-independent peak stretch behavior was observed. In contrast, when $\tau_\lambda \gg \tau_{\rm v}$, the material exhibits low modulus with minimal rate dependence in the pre-failure response. However, once damage initiates, crack propagation becomes highly rate-dependent due to viscous effects in the process zone. This behavior, captured by the model with appropriate parameter selection, closely matches experimental observations on polyurethane elastomers reported in Cristiano et al. (2011).

The ability to reproduce these distinct time-scale effects stems from the model's separate treatment of material and damage characteristic times, underscoring the importance of this key feature of the formulation. The current model serves as an initial framework to exploit these internal time scales. Future enhancements should consider non-Gaussian strain energies to reproduce the transition from entropic to enthalpic elasticity, as well as all nonlinear viscosities, such as shear-thinning viscosity, which are relevant for accurately describing the mechanics of elastomers. However, extension of these modeling improvements to regimes of extreme deformations and strain rates attained at the crack tip remains an ongoing challenge, particularly given that the micromechanical behavior of elastomers near the fracture tip is not clearly understood from an experimental standpoint. Addressing this gap would facilitate the transition from the proposed phenomenological model to a physically based formulation.

CRediT authorship contribution statement

Jacopo Ciambella: Writing – original draft, Visualization, Validation, Software, Methodology, Investigation, Formal analysis, Data curation, Conceptualization. **Giovanni Lancioni:** Writing – original draft, Visualization, Validation, Software, Methodology, Investigation, Formal analysis, Data curation, Conceptualization. **Nico Stortini:** Writing – original draft, Visualization, Validation, Software, Methodology, Investigation, Formal analysis, Data curation, Conceptualization.

Declaration of competing interest

The authors declare the following financial interests/personal relationships which may be considered as potential competing interests: Giovanni Lancioni reports financial support was provided by MUR - PRIN funded Program 2022YFTS7N. If there are other authors, they declare that they have no known competing financial interests or personal relationships that could have appeared to influence the work reported in this paper.

Acknowledgments

Authors wish to acknowledge the financial support of PRIN funded Program 2022YFTS7N, "TWYRES: a digital TWin for fracture and fatigue simulations in tYRES". The research leading to this paper was carried out under the auspices of the Italian INdAM-GNFM.

Appendix. Numerical solution scheme

Problem for $\dot{\mathbf{u}}$. The displacement rate $\dot{\mathbf{u}}$ is determined by the sum $\dot{\mathbf{u}}^j = \dot{\mathbf{u}}^{j-1} + \delta\dot{\mathbf{u}}$, where $\dot{\mathbf{u}}^{j-1}$ is the displacement rate evaluated in the previous iterative step, and the increment $\delta\dot{\mathbf{u}}$ is the solution of the linear balance equation

$$\mathrm{Div}\left(\frac{\partial \mathbf{P}(\nabla\dot{\mathbf{u}}^{j-1})}{\partial \nabla\mathbf{u}}[\nabla\delta\dot{\mathbf{u}}]\right) + \mathrm{Div}\,\mathbf{P}(\nabla\dot{\mathbf{u}}^{j-1}) + \mathbf{b} = 0, \tag{A.1}$$

obtained from (6) by developing $\mathbf{P}$ up to the first-order with respect to $\delta\dot{\mathbf{u}}$, and keeping $\dot{d}$ and $\dot{\mathbf{C}}_{\rm v}$ fixed. Eq. (A.1) is solved in weak form according to standard finite elements procedure.

Problem for $\dot{d}$. The phase-field rate $\dot{d}$ is determined by minimizing the internal energy increment (3), keeping $\dot{\mathbf{u}}$ and $\dot{\mathbf{C}}_{\rm v}$ fixed, and imposing the constrain $\dot{d} \geq 0$. The resulting constrained programming problem is equivalent to equation $(23)_2$, and it is solved by using the *quadprog* routine in Matlab.

Problem for $\dot{\mathbf{C}}_{\rm v}$. The evolution equation in 1 for the viscous strain is solved using an explicit fifth-order Runge–Kutta scheme (Lawson, 1966; Kumar and Lopez-Pamies, 2016).

At each time step, the above problems are iteratively solved in the numerical code, according to following procedure, with assigned tolerances tol_d and $\mathrm{tol}_{\mathbf{u}}$.

- Update boundary conditions.
- Initialize $i = 0$, $j = 0$, and $(\dot{\mathbf{u}}_i^j,\ d_i^j,\ \dot{\mathbf{C}}_{{\rm v}\,i}^j) = (\mathbf{0},\ 0,\ \mathbf{0})$.
- Iterations for i.
  - * Update $i = i + 1$.
  - * Iterations for j.
    - → Update $j = j + 1$.
    - → Solve ($\dot{\mathbf{u}}$ *Pb.*) to find $\dot{\mathbf{u}}_i^j$, and update $\mathbf{u}_i^j = \mathbf{u}_t + \tau\dot{\mathbf{u}}_i^j$.
    - → Solve ($\dot{\mathbf{C}}_{\rm v}$ *Pb.*) to find $\dot{\mathbf{C}}_{{\rm v}\,i}^j$, and update $\mathbf{C}_{{\rm v}\,i}^j = \mathbf{C}_{{\rm v}\,t} + \tau\dot{\mathbf{C}}_{{\rm v}\,i}^j$.
    - → If $|\dot{\mathbf{u}}_i^{j-1} - \dot{\mathbf{u}}_i^j|_\infty < \mathrm{tol}_{\mathbf{u}}$, stop iteration for j.
  - * Solve ($\dot{d}$ *Pb.*) to find $\dot{d}_i$, and update $d_i = d_t + \tau\dot{d}_i$.
  - * If $|d_i^j - d_{i-1}^j|_\infty < \mathrm{tol}_d$, stop iteration for i.
- Assign $(\mathbf{u}_{t+\tau}, d_{t+\tau}, \mathbf{C}_{{\rm v}\,t+\tau}) = (\mathbf{u}_i^j, d_i, \mathbf{C}_{{\rm v}\,i}^j)$.

In the numerical code, the domain is discretized through three-nodes triangular elements, and, within each element, the fields $\mathbf{u}$ and d are approximated by linear shape-functions, and $\mathbf{C}_v$ is assumed homogeneous. The tolerances used in the simulations are set to $\mathrm{tol}_d = \mathrm{tol}_{\mathbf{u}} = 10^{-3}$, and the mesh size in the refined region is 0.1, which is ten times smaller than the fracture bandwidth $\ell_f = 1$.

Data availability

Data will be made available on request.

References

Ambrosio, L., Tortorelli, V.M., 1990. Approximation of functional depending on jumps by elliptic functional via t-convergence. Comm. Pure Appl. Math. 43 (8), 999–1036. http://dx.doi.org/10.1002/cpa.3160430805.

Barthel, E., 2024. The linear viscoelastic fracture theory applies to soft solids better when they are...viscoelastic. Proc. R. Soc. A Math. Phys. Eng. Sci. 480 (2288), http://dx.doi.org/10.1098/rspa.2023.0561.

Bourdin, B., Francfort, G.A., Marigo, J.J., 2000. Numerical experiments in revisited brittle fracture. J. Mech. Phys. Solids 48 (4), 797–826. http://dx.doi.org/10.1016/s0022-5096(99)00028-9.

Califano, F., Ciambella, J., 2023. Viscoplastic simple shear at finite strains. Proc. R. Soc. A Math. Phys. Eng. Sci. 479 (2280), http://dx.doi.org/10.1098/rspa.2023.0603.

Chen, C.H., Zhang, H.P., Niemczura, J., Ravi-Chandar, K., Marder, M., 2011. Scaling of crack propagation in rubber sheets. Epl 96 (3), http://dx.doi.org/10.1209/0295-5075/96/36009.

Ciambella, J., Lancioni, G., Stortini, N., 2022. An ogden-like formulation incorporating phase-field fracture in elastomers: from brittle to pseudo-ductile failures. Phil. Trans. R. Soc. A 380 (2234), 20210323.

Ciambella, J., Lucci, G., Nardinocchi, P., 2024. Anisotropic evolution of viscous strain in soft biological materials. Mech. Mater. 192, 104976. http://dx.doi.org/10.1016/j.mechmat.2024.104976.

Ciavarella, M., 2024. Discussion: A comment on "The trousers fracture test for viscoelastic elastomers" (Shrimali, B., and Lopez-Pamies, O., 2023, ASME J. Appl. Mech., 90(7), p. 071010). J. Appl. Mech. Trans. ASME 91 (5), 1–4. http://dx.doi.org/10.1115/1.4064126.

Corre, T., Coret, M., Verron, E., Leblé, B., Le Lay, F., 2020. Experimental full field analysis for dynamic fracture of elastomer membranes. Int. J. Fract. 224 (1), 83–100.

da Costa-Haveroth, T.C., Haveroth, G.A., Bittencourt, M.L., Boldrini, J.L., 2022. A damage phase-field model for fractional viscoelastic materials in finite strain. Comput. Mech. 69 (6), 1365–1393. http://dx.doi.org/10.1007/s00466-022-02145-2.

Creton, C., Ciccotti, M., 2016. Fracture and adhesion of soft materials: a review. Rep. Progr. Phys. 79 (4), 046601.

Cristiano, A., Marcellan, A., Keestra, B.J., Steeman, P., Creton, C., 2011. Fracture of model polyurethane elastomeric networks. J. Polym. Sci. B Polym. Phys. 49 (5), 355–367. http://dx.doi.org/10.1002/polb.22186.

Cui, H.R., Li, H.Y., Shen, Z.B., 2019. Cohesive zone model for mode-I fracture with viscoelastic-sensitivity. Eng. Fract. Mech. 221 (December 2018), 106578. http://dx.doi.org/10.1016/j.engfracmech.2019.106578.

Dammaß, F., Ambati, M., Kästner, M., 2021. A unified phase-field model of fracture in viscoelastic materials. Contin. Mech. Thermodyn. 33 (4), 1907–1929. http://dx.doi.org/10.1007/s00161-021-01013-3.

Dammaß, F., Kalina, K.A., Ambati, M., Kästner, M., 2023. Phase-field modelling and analysis of rate-dependent fracture phenomena at finite deformation. Comput. Mech. 72 (5), 859–883. http://dx.doi.org/10.1007/s00466-023-02310-1.

Del Piero, G., Lancioni, G., March, R., 2007. A variational model for fracture mechanics: Numerical experiments. J. Mech. Phys. Solids 55 (12), 2513–2537. http://dx.doi.org/10.1016/j.jmps.2007.04.011.

Del Piero, G., Lancioni, G., March, R., 2013. A diffuse cohesive energy approach to fracture and plasticity: the one-dimensional case. J. Mech. Mater. Struct. 8 (2), 109–151.

Del Piero, G., Lancioni, G., March, R., 2023. One-dimensional failure modes for bodies with non-convex plastic energies. J. Elasticity 153 (2), 275–298. http://dx.doi.org/10.1007/s10659-023-09989-6.

Francfort, G.A., Marigo, J.J., 1998. Revisiting brittle fracture as an energy minimization problem. J. Mech. Phys. Solids 46 (8), 1319–1342. http://dx.doi.org/10.1016/s0022-5096(98)00034-9.

Halphen, B., Son, Q., Sur, N., 1975. Sur les matériaux standard généralisés. J. Méc. 14 (1), 39–63.

Henao, D., Mora-Corral, C., Xu, X., 2016. A numerical study of void coalescence and fracture in nonlinear elasticity. Comput. Methods Appl. Mech. Engrg. 303, 163–184. http://dx.doi.org/10.1016/j.cma.2016.01.012.

Ichiyanagi, M., 1994. Variational principles of irreversible processes. Phys. Rep. 243 (3), 125–182. http://dx.doi.org/10.1016/0370-1573(94)90085-6.

Kamarei, F., Sozio, F., Lopez-Pamies, O., 2024. The single edge notch fracture test for viscoelastic elastomers. arXiv:2410.15380 URL http://arxiv.org/abs/2410.15380.

Kamasamudram, V., Coret, M., Moës, N., 2021. The role played by viscoelasticity in the bulk material during the propagation of a dynamic crack in elastomers. Int. J. Fract. 231 (1), 59. http://dx.doi.org/10.1007/s10704-021-00561-8.

Knauss, W.G., 1970. Delayed failure - the Griffith problem for linearly viscoelastic materials. Int. J. Fract. Mech. 6 (1), 7–20. http://dx.doi.org/10.1007/bf00183655.

Knauss, W.G., 2015. A review of fracture in viscoelastic materials. Int. J. Fract. 196 (1–2), 99–146. http://dx.doi.org/10.1007/s10704-015-0058-6.

Kubo, A., Sakumichi, N., Morishita, Y., Okumura, K., Tsunoda, K., Urayama, K., Umeno, Y., 2021. Dynamic glass transition dramatically accelerates crack propagation in rubberlike solids. Phys. Rev. Mater. 5 (7), 1–14. http://dx.doi.org/10.1103/PhysRevMaterials.5.073608.

Kubo, A., Umeno, Y., 2017. Velocity mode transition of dynamic crack propagation in hyperviscoelastic materials: A continuum model study. Sci. Rep. 7 (September 2016), 4–6. http://dx.doi.org/10.1038/srep42305.

Kumar, A., A. Francfort, G., Lopez-Pamies, O., 2018. Fracture and healing of elastomers: A phase-transition theory and numerical implementation. J. Mech. Phys. Solids 112, 523–551. http://dx.doi.org/10.1016/j.jmps.2018.01.003.

Kumar, A., Lopez-Pamies, O., 2016. On the two-potential constitutive modeling of rubber viscoelastic materials. C. R. Mec. 344 (2), 102–112.

Lancioni, G., Royer-Carfagni, G., 2009. The variational approach to fracture mechanics. a practical application to the french panthéon in Paris. J. Elasticity 95 (1–2), 1–30. http://dx.doi.org/10.1007/s10659-009-9189-1.

Lawson, J.D., 1966. An order five Runge-Kutta process with extended region of stability. SIAM J. Numer. Anal. 3 (4), 593–597.

Li, B., Bouklas, N., 2020. A variational phase-field model for brittle fracture in polydisperse elastomer networks. Int. J. Solids Struct. 182–183, 193–204. http://dx.doi.org/10.1016/j.ijsolstr.2019.08.012.

Loew, P.J., Peters, B., Beex, L.A., 2019. Rate-dependent phase-field damage modeling of rubber and its experimental parameter identification. J. Mech. Phys. Solids 127, 266–294.

Mai, T.T., Okuno, K., Tsunoda, K., Urayama, K., 2020. Crack-tip strain field in supershear crack of elastomers. ACS Macro Lett. 9 (5), 762–768. http://dx.doi.org/10.1021/acsmacrolett.0c00213.

Mai, T.T., Okuno, K., Tsunoda, K., Urayama, K., 2021. Anisotropic stress-softening effect on fast dynamic crack in filler-reinforced elastomers. Mech. Mater. 155 (November 2020), 103786. http://dx.doi.org/10.1016/j.mechmat.2021.103786.

Miehe, C., 2011. A multi-field incremental variational framework for gradient-extended standard dissipative solids. J. Mech. Phys. Solids 59 (4), 898–923. http://dx.doi.org/10.1016/j.jmps.2010.11.001.

Miehe, C., Schänzel, L.-M., 2014. Phase field modeling of fracture in rubbery polymers. Part I: Finite elasticity coupled with brittle failure. J. Mech. Phys. Solids 65, 93–113.

Miehe, C., Welschinger, F., Hofacker, M., 2010. Thermodynamically consistent phase-field models of fracture: Variational principles and multi-field FE implementations. Internat. J. Numer. Methods Engrg. 83 (10), 1273–1311. http://dx.doi.org/10.1002/nme.2861.

Morishita, Y., Tsunoda, K., Urayama, K., 2016. Velocity transition in the crack growth dynamics of filled elastomers: Contributions of nonlinear viscoelasticity. Phys. Rev. E 93 (4), 1–11. http://dx.doi.org/10.1103/PhysRevE.93.043001.

Nguyen, T.D., Govindjee, S., 2006. Numerical study of geometric constraint and cohesive parameters in steady-state viscoelastic crack growth. Int. J. Fract. 141 (1–2), 255–268. http://dx.doi.org/10.1007/s10704-006-0080-9.

Persson, B.N., Albohr, O., Heinrich, G., Ueba, H., 2005. Crack propagation in rubber-like materials. J. Phys.: Condens. Matter. 17 (44), http://dx.doi.org/10.1088/0953-8984/17/44/r01.

Persson, B.N., Brener, E.A., 2005. Crack propagation in viscoelastic solids. Phys. Rev. E (3) 71 (3), 1–8. http://dx.doi.org/10.1103/PhysRevE.71.036123.

Persson, B.N., Carbone, G., Creton, C., Heinrich, G., Tada, T., 2024. Some comments on the fracture of viscoelastic solids. Extrem. Mech. Lett. 68 (September 2023), 102143. http://dx.doi.org/10.1016/j.eml.2024.102143.

Pharr, M., Sun, J.-Y., Suo, Z., 2012. Rupture of a highly stretchable acrylic dielectric elastomer. J. Appl. Phys. 111 (10), 104114. http://dx.doi.org/10.1063/1.4721777.

Qi, Y., Li, X., Venkata, S.P., Yang, X., Sun, T.L., Hui, C.-y., Gong, J.P., Long, R., 2024. Mapping deformation and dissipation during fracture of soft viscoelastic solid. J. Mech. Phys. Solids 186 (March), 105595. http://dx.doi.org/10.1016/j.jmps.2024.105595.

Reese, S., Govindjee, S., 1998. A theory of finite viscoelasticity and numerical aspects. Int. J. Solids Struct. 35 (26–27), 3455–3482.

Sadik, S., Yavari, A., 2023. Nonlinear anisotropic viscoelasticity. J. Mech. Phys. Solids 105461. http://dx.doi.org/10.1016/j.jmps.2023.105461.

Schapery, R.A., 1975. A theory of crack initiation and growth in viscoelastic media - I. Theoretical development. Int. J. Fract. 11 (1), 141–159. http://dx.doi.org/10.1007/bf00034721.

Schapery, R.A., 2022. Stable and unstable viscoelastic crack growth: experimental validation of nonlinear theory for rubber. Int. J. Fract. 238 (1), 1–15. http://dx.doi.org/10.1007/s10704-022-00639-x.

Schapery, R.A., 2023. Crack growth in viscoelastic media with large strains: further results and validation of nonlinear theory for rubber. Int. J. Fract. 241 (2), 121–139. http://dx.doi.org/10.1007/s10704-023-00696-w.

Shrimali, B., Lopez-Pamies, O., 2023a. The delayed fracture test for viscoelastic elastomers. Int. J. Fract. 242 (1), 23–38. http://dx.doi.org/10.1007/s10704-023-00700-3.

Shrimali, B., Lopez-Pamies, O., 2023b. The "pure-shear" fracture test for viscoelastic elastomers and its revelation on Griffith fracture. Extrem. Mech. Lett. 58, 101944. http://dx.doi.org/10.1016/j.eml.2022.101944.

Shrimali, B., Lopez-Pamies, O., 2023c. The trousers fracture test for viscoelastic elastomers. J. Appl. Mech. Trans. ASME 90 (7), 1–10. http://dx.doi.org/10.1115/1.4062140.

Talamini, B., Mao, Y., Anand, L., 2018. Progressive damage and rupture in polymers. J. Mech. Phys. Solids 111, 434–457.

Treloar, L., 2005. The Physics of Rubber Elasticity. Clarendon Press, Oxford.

Wang, H., Wang, K., Fan, W., Cai, S., 2017. Rupture of swollen styrene butadiene rubber. Polym. Test. 61, 100–105. http://dx.doi.org/10.1016/j.polymertesting.2017.05.019.

Wang, J., Zhu, B., Hui, C.Y., Zehnder, A.T., 2023. Delayed fracture caused by time-dependent damage in PDMS. J. Mech. Phys. Solids 181 (September), 105459. http://dx.doi.org/10.1016/j.jmps.2023.105459.

Yin, B., Kaliske, M., 2020. Fracture simulation of viscoelastic polymers by the phase-field method. Comput. Mech. 65 (2), 293–309. http://dx.doi.org/10.1007/s00466-019-01769-1.

Zreid, I., Fleischhauer, R., Kaliske, M., 2013. A thermomechanically coupled viscoelastic cohesive zone model at large deformation. Int. J. Solids Struct. 50 (25–26), 4279–4291. http://dx.doi.org/10.1016/j.ijsolstr.2013.08.031.